Check for updates

Metal–organic frameworks and their derivatives for the electrochemical CO$_2$ reduction reaction: insights from molecular engineering

Xiaoming Liu, [ID] [a] Xuan-He Liu, [ID] *[a] Xiangrui Zhang,[a] Huan Wang [ID] [b] and Qinglan Zhao [ID] *[c]

Excessive fossil fuel consumption has led to a rapid increase in CO$_2$ concentration, posing a threat to the global environment. The electrochemical conversion of CO$_2$ back into valuable carbon-containing products offers a promising solution; however the lack of efficient electrocatalysts remains a challenge for high-efficiency CO$_2$ reduction reaction (CO$_2$RR). Metal–organic frameworks (MOFs) have emerged as promising electrocatalysts owing to their superior activity and well-defined active sites and are recognized as model electrocatalysts for the fundamental study of electrocatalytic reaction mechanisms. In this review, focusing on the roles of metals and the coordination environment, we have discussed the molecular engineering of MOF electrocatalysts for the CO$_2$RR, including regulation of metal nodes, modulation of surrounding organic ligands, and post-modification of MOFs. In addition, stability of MOFs and transformation strategies through the wet chemistry method and pyrolysis treatment to obtain MOF derivatives are summarized. Metal centers and the coordination environment of N atoms and other heteroatoms of MOF derivatives are discussed for their performance in the CO$_2$RR. Furthermore, computational simulations and advanced characterization studies are also summarized to understand the correlation between the structure and performance of MOFs and their derivatives. By overviewing the progress and current challenges of MOF electrocatalysts and their derivatives for the CO$_2$RR, we are aiming to provide insights into design principles and propose future directions for high-efficiency electrocatalysts, paving the way toward carbon neutrality.

1. Introduction

Since the industrial revolution, there has been a dramatic increase in human demand for energy,[1] leading to a great energy crisis. Furthermore, the excessive consumption of fossil fuels such as coal, oil and natural gas has resulted in a rapid increase in the global concentration of CO$_2$ and related environmental issues.[2] For example, the high concentration of greenhouse gases reduces the infrared radiation emitted into space, leading to the warming of the earth, melting glaciers, and ultimately an increase in sea levels.[3] As a result, the concept of carbon neutrality was proposed by the Paris Agreement,[4] to convert the released CO$_2$ back to carbon products to achieve net zero emission by 2050.

In recent decades, tremendous efforts have been dedicated to CO$_2$ conversion with various strategies including photo-chemical,[5] thermochemical,[6] biochemical,[7,8] chemical reforming,[9–11] mineralization,[12] electrochemical[13–15] methods, and so on. Among these, the electrochemical CO$_2$ reduction reaction (CO$_2$RR) stands out as a promising approach to achieving carbon neutrality, as it can be conducted under mild aqueous solution conditions with the input of renewable electricity.[16,17] In this regard, numerous constructive research studies have been reported to achieve high-performance electrocatalytic CO$_2$RR toward formation of valuable reduced carbon products, by enhancing selectivity,[18,19] energy efficiency,[20,21] and stability.[22,23] In the past few years, significant efforts have been devoted to developing efficient electrocatalysts for the CO$_2$RR, such as metal nanoparticles (*e.g.*, Ag, Au, Cu, Zn and Sn),[24–29] metal complexes (*e.g.*, oxides, sulfides and nitrides),[30–32] carbonaceous materials,[33] and metal–organic frameworks.[34,35]

Metal–organic frameworks (MOFs), a type of crystalline porous material with a periodic network structure formed by the self-assembly of transition metal ions and organic ligands, have been intensively studied as electrocatalysts for the CO$_2$RR[36,37] due to their large specific surface area, tunable structure and

[a]School of Science, China University of Geosciences (Beijing), Beijing 100083, China. E-mail: liuxh@cugb.edu.cn

[b]Key Laboratory of Advanced Energy Materials Chemistry (Ministry of Education), Nankai University, Tianjin 300071, China

[c]Department of Chemical and Biological Engineering, The Hong Kong University of Science and Technology, Clear Water Bay, Kowloon, Hong Kong, China. E-mail: keqzhao@ust.hk
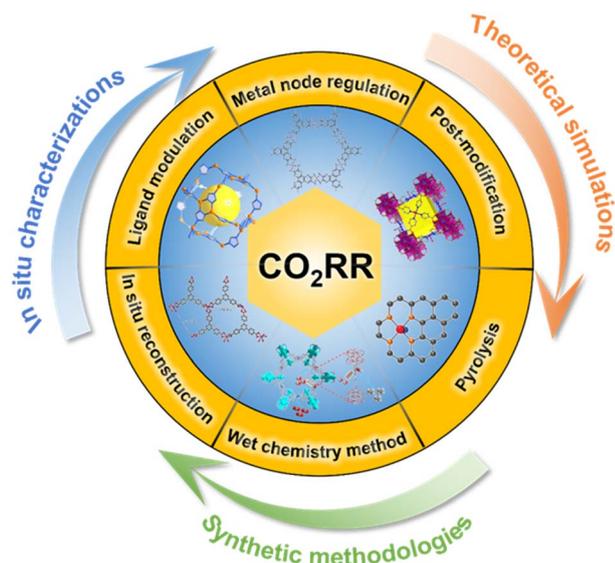
Fig. 1 Scheme of the molecular engineering strategy including regulation of metal nodes, modulation of surrounding organic ligands and post-modification of MOFs; *in situ* characterization and reconstruction; the wet chemistry method and pyrolysis treatment for MOF derivatives for the CO_2RR (molecular structures shown in the scheme have been cited from ref. 49–54 with copyright approval from Wiley-VCH and American Chemical Society).

ordered structure.[38] Furthermore, their well-defined structures and uniform active centers make it easy to construct reliable structural models to understand the mechanism of the CO_2RR.[39,40] It has been reported that both metal species[41,42] and organic linkers[43,44] of MOFs can serve as active sites or modifiers to drive electrocatalytic reactions. Besides MOFs, MOF-derived electrocatalysts, especially those with precisely active centers, also play a crucial role in influencing CO_2RR activity and selectivity through the manipulation of the electronic structure.[45–48]

Based on the understanding of the roles of active metal nodes and coordinating organic ligands of MOF electrocatalysts, we discuss the molecular engineering strategy including regulation of metal nodes, modulation of surrounding organic ligands, and post-modification of MOFs for the CO_2RR (Fig. 1). Regarding MOF derivatives, we discuss transformation strategies including the wet chemistry method at mild temperature and pyrolysis treatment at high temperature. In particular, the significant impacts of metal centers and the coordination environment surrounded by N atoms and other heteroatoms on performance of the CO_2RR are discussed. Advanced structural characterization studies combined with the first-principle density functional theory (DFT) calculations to unravel the active sites for MOFs at atomic and molecular levels are summarized to help understand the relationship between their structure and performance.[55–58] Finally, the current challenges and future directions are proposed for advancing MOF-based electrocatalysts for the CO_2RR.

2. Fundamentals of the CO_2 reduction reaction

The σ and π_3^4 bonds of linear CO_2 molecules endow the C=O bond with a certain degree of triple-bond character, which is thermodynamically stable and chemically inert.[3] Therefore, the CO_2RR is typically kinetically sluggish,[59] especially toward high-energy and value-added carbon products formation with multi-proton and multi-electron transfer steps, such as CH_4 ($8e^-$), CH_3OH ($6e^-$), C_2H_4 ($12e^-$), and C_2H_5OH ($12e^-$).[60] Up to now, at least 16 products have been identified in the CO_2RR, with their corresponding half reactions listed in Table 1,[61–63] leading to the occurrence of complex reactions yielding various carbon products. Moreover, the hydrogen evolution reaction (HER) with an equilibrium potential of 0 V *vs.* the reversible hydrogen electrode (RHE) hinders the CO_2RR as a competition reaction.

Table 1 The half reactions of the CO_2RR and corresponding equilibrium potentials at a pH of 6.8 *vs.* RHE calculated from tabulated thermodynamic data in aqueous solution

Half reactions	Equilibrium potentials (V *vs.* RHE)	Number
$CO_2 + 2H^+ + 2e^- \rightarrow HCOOH$ (aq)	−0.02	(1)
$CO_2 + 2H^+ + 2e^- \rightarrow CO$ (g) $+H_2O$ (l)	−0.10	(2)
$CO_2 + 8H^+ + 8e^- \rightarrow CH_4$ (g) $+ 2H_2O$ (l)	0.17	(3)
$CO_2 + 4H^+ + 4e^- \rightarrow HCHO$ (aq) $+ H_2O$ (l)	−1.31	(4)
$CO_2 + 4H^+ + 4e^- \rightarrow C$ (s) $+ H_2O$ (l)	0.21	(5)
$CO_2 + 6H^+ + 6e^- \rightarrow CH_3OH$ (aq) $+H_2O$ (l)	0.03	(6)
$2CO_2 + 12H^+ + 12e^- \rightarrow C_2H_4$ (g) $+ 4H_2O$ (l)	0.08	(7)
$2CO_2 + 12H^+ + 12e^- \rightarrow C_2H_5OH$ (aq) $+ 3H_2O$ (l)	0.09	(8)
$2CO_2 + 8H^+ + 8e^- \rightarrow CH_3COOH$ (aq) $+ 2H_2O$ (l)	−0.26	(9)
$2CO_2 + 10H^+ + 10e^- \rightarrow CH_3CHO$ (aq) $+ 3H_2O$ (l)	0.05	(10)
$2CO_2 + 14H^+ + 14e^- \rightarrow C_2H_6$ (aq) $+ 4H_2O$ (l)	0.14	(11)
$2CO_2 + 2H^+ + 2e^- \rightarrow H_2C_2O_4$ (aq)	−0.91	(12)
$2CO_2 + 16H^+ + 16e^- \rightarrow C_2H_5CHO$ (aq) $+ 5H_2O$ (l)	0.14	(13)
$3CO_2 + 18H^+ + 18e^- \rightarrow C_2H_5CH_2OH$ (aq) $+ 5H_2O$ (l)	0.21	(14)
$3CO_2 + 20H^+ + 20e^- \rightarrow C_3H_8$ (g) $+ 6H_2O$ (l)	0.09	(15)
$3CO_2 + 16H^+ + 16e^- \rightarrow (CH_3)_2CO$ (aq) $+ 5H_2O$ (l)	−0.26	(16)
$2H^+ + 2e^- \rightarrow H_2$ (g)	0	(17)

This journal is © The Royal Society of Chemistry 2024

J. Mater. Chem. A, 2024, **12**, 20578–20605 | **20579**

Table 2 Summary of CO_2RR products over recently reported MOF-based electrocatalysts

Sample	Main product	FE (%)	Potential (V vs. RHE)	Stability (h)	Ref.
Ag@UiO-66-SH	CO	74.0	−1.10	10	64
Fe_2–N_6–C-o	CO	>80.0	−0.5 to −0.9	21	65
ZIF-8	CO	81.0	−1.10	—	66
CoPc–Cu–O	CO	85.0	−0.63	10	67
PcCu–O_8–Zn	CO	88.0	−0.70	>10	68
$Cu_{0.5}Zn_{0.5}$/ZIF-8	CO	88.5	−1.00	>6	69
Fe@BIF-73-NS	CO	88.6	−1.8 V vs. Ag/AgCl	14	70
ZIF-A-LD	CO	90.57	−1.10	10	71
Zr-BTB@Hemin-TMA	CO	92.0	−1.20	3.0	72
Ga–N_3S–PC	CO	92.0	−0.30	24	73
NCMSH	CO	92.68	−0.70	>24	74
Fe–N_{2+2}–C_8	CO	93.0	−0.47	20	75
Fe–N_5/DPCF	CO	93.1	−0.50	25	76
Ag/Zr-*fcu*-MOF-NDC	CO	94.0	−1.00	1	77
CALF20	CO	94.5	−0.97	~2.2	78
Co–N_2	CO	95.0	−0.68	60	79
O–Fe–N–C	CO	95.0	−0.50	30	54
Ni-SNC	CO	95.0	−0.80	24	80
Bi-BTC-D	CO	95.5	−0.86	12	81
Ni–N_3–C	CO	95.6	−0.65	10	48
1-NH_2	CO	96.0	−2.30	300	82
CuN_3O/C	CO	96.0	−0.80	15	83
Fe_1–Ni_1–N–C	CO	96.2	−0.50	10	46
$CoCp_2$@MOF-545-Co	CO	97.0	−0.70	8	84
Ni/HNC	CO	97.2	−0.70	10	85
ZIF–NC–Ni–Fe	CO	97.8	−0.60	50	86
NiSA–N_2–C	CO	98.0	−0.80	10	34
Cu–Fe–N_6–C	CO	98.0	−0.70	10	87
S/Fe–poN_4–C	CO	98.2	−0.58	>12	88
MOF Ni–Fe	CO	98.2	−0.50	30	50
Ni SAC-1000	CO	98.24	−0.80	24	89
NiPc–NiO_4	CO	98.4	−0.85	10	90
K-defect-C-1100	CO	99.0	−0.45	10	91
Fe/Cu–N–C	CO	~99.0	−0.80	60	92
Fe–S_1N_3	CO	99.02	−0.50	40	47
Ni/Cu–N–C	CO	99.2	−0.79	60	93
FeTCPP⊂UiO-66	CO	~100	−0.56	2.5	94
H-3DOM-ZnN_4/P–C	CO	~100	−0.60	>30	95
ZnN_4S_1/P-HC	CO	~100	−0.60	>30	96
Bi/UiO-66	HCOOH	70–85	−0.4 to −0.7	1.1	97
In-BDC	$HCOO^-$	88.0	−0.669	21	98
$(Me_2NH_2^+)${In^{III}-[$Ni(C_2S_2(C_6H_4COO)_2)_2$]}·3DMF·1.5$H_2O$	$HCOO^-$	89.6	−1.30	12	99
Bi-HHTP	HCOOH	90.0%	2.60 (cell voltage)	>30	100
FJU-127-CH_3	$HCOO^-$	90.2	−1.57	5	101
Bi-ZMOF	HCOOH	91.0	−1.10	12	102
BiZn-MOF	$HCOO^-$	92.0	−0.90	13	103
Bi NS	$HCOO^-$	92.0	−1.10	10	104
$Sb_{2.5}$/Bi@C	HCOOH	94.8	−1.40	30	105
Bi(btb)	$HCOO^-$	95.0	−0.97	32	52
Bi-HHTP	$HCOO^-$	>95.0	−0.70	>30	106
CAU-17 MOFs	HCOOH	95.5	−1.10	10	107
Bi-BTC	$HCOO^-$	96.0	−0.90	24	108
Ce_2–Bi@C	$HCOO^-$	97.2	−1.10	48	109
$In_2O_{3−x}$@C	HCOOH	98.0	−1.20	120	110
Bi-ene	$HCOO^-$	~100	−0.8 to −1.2	12	111
Cu-PorOH	CH_4	51.3	−1.50	6	112
Cu/a-C	CH_4	55.0	−1.40	12.5	113
Cu-DBC	CH_4	56.0	−1.40	4	114
Cu–I	CH_4	57.2	−1.08	10	58
Cu_2O@Cu-MOF	CH_4	63.2	−1.71	1	115
2D-vc-MOF(Cu)	CH_4	65.0	−1.40	4	116
MCH-3	CH_4	76.7	−1.00	100 min	117
HATNA-Cu-MOF	CH_4	78.0	−1.50	12	118

20580 | J. Mater. Chem. A, 2024, 12, 20578–20605

This journal is © The Royal Society of Chemistry 2024

Table 2 (*Contd.*)

| Sample	Main product	FE (%)	Potential (V vs. RHE)	Stability (h)	Ref.
Cu/CeO$_2$@C	CH$_4$	80.3	−1.50	9	119
2Bn-Cu@ UiO-67	CH$_4$	81.0	−1.50	6 min	120
Cu$_4$-MFU-4l	CH$_4$	92.0	−1.20	24	121
BIF-102NSs	C$_2$H$_4$	11.3	−1.00	5	122
Fe-TCPP@Cu	C$_2$H$_4$	33.42	−1.17	5	123
CuN$_2$/Cu(111)	C$_2$H$_4$	41.5	—	6	124
Cu–MOF–CF	C$_2$H$_4$	48.6	−1.10	12	125
C/HKUST-1/Cu/PTFE	C$_2$H$_4$	54.0	−4.00	65	126
PcCu–Cu–O	C$_2$H$_4$	50.0	−1.20	4	127
Cutrz	C$_2$H$_4$	50.0	−1.20	80	128
Cu-HITP@PDA	C$_2$H$_4$	51.0	−1.20	10	129
MAF-2E, MAF-2E MAF-2P	C$_2$H$_4$	51.2 ± 2.3	−1.10−1.50	10	49
CuTrz-109	C$_2$H$_4$	55.4	−1.15	10	130
Ag/Cu/Cu$_2$OAg$_{0.1}$/HKUST-1	C$_2$H$_4$	57.2	−1.30	10	131
S-HKUST-1	C$_2$H$_4$	60.0 ± 2.0	−1.32	8	132
KB@Cu$_3$(HITP)$_2$	C$_2$H$_4$	70.0	−1.37	10	133
Cu–SAs@Ir–PCN-222-PA	C$_2$H$_4$	70.9	−1.00	16	53
CuPz$_2$-Act-30	C$_2$H$_4$	70.2 ± 1.7	−1.03	12	134
Cu–Cu$_2$O@CC	CH$_3$OH	37.4	−0.70	6	135
OD-Cu/C	CH$_3$OH	∼43.2	−0.30	15	136
Cu@Cu$_2$O-400 °C	CH$_3$OH	45.0	−0.70	10	137
Cu$_3$(HHTQ)$_2$	CH$_3$OH	53.6	−0.40	10	138
CuNi SAs/UiO-66(Hf)	CH$_3$OH	∼98.0	—	—	139
Cutrz	CH$_3$COOH	2.20	−1.20	80	128
CuN$_2$/Cu(111)	C$_2$H$_5$OH	18.2	—	6	124
Cutrz	C$_2$H$_5$OH	19.7	−1.20	80	128
Cu-MMT–H$_2$O	C$_2$H$_5$OH	20.8	−1.15	—	140
Cu$_{2−x}$Se-450	C$_2$H$_5$OH	42.0	−0.74	—	141
CuAg$_5$@NC	C$_2$H$_5$OH	51.8	−1.00	20	142
CuSn–HAB	C$_2$H$_5$OH	56.0	−0.57	65	143
OM–Cu–NiSNC	C$_2$H$_5$OH	63.0	−0.76	50	144
Cu GNC-VL	C$_2$H$_5$OH	70.52	−0.87	12	145
Cu$_2$N$_4$/Cu(111)	n-C$_3$H$_7$OH	3.40	—	6	124
CuN$_2$/Cu(111)	n-C$_3$H$_7$OH	5.10	—	6	124
Cu–SA/NPC	CH$_3$COCH$_3$	36.70	−0.36	10	146
Cu$_{0.85}$Zn$_{0.15}$/C	CH$_3$COCH$_3$	38.10	−0.40	—	147
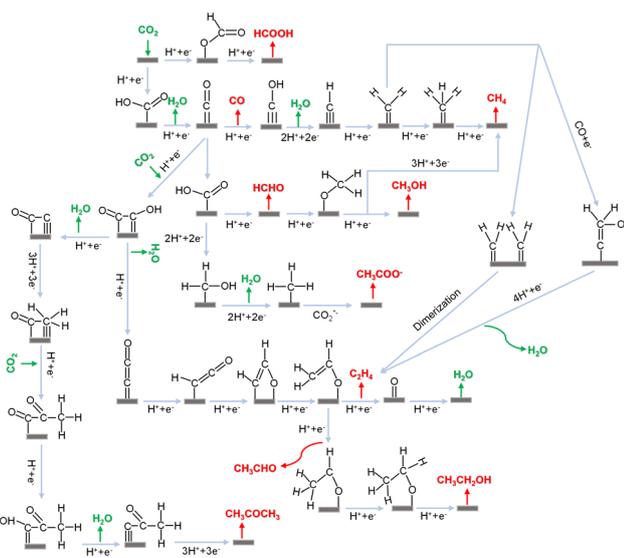
Fig. 2 Possible pathways of the CO$_2$RR toward various reduction products.

Therefore, it is a significant challenge to achieve certain desired reduction products with high selectivity and activity.

As summarized in Table 2, CO and HCOOH in 2-electron transfer reactions are common reduction products, whose faradaic efficiencies (FEs) reach up to 100% in MOF-based catalysts.[50,81,90,110] However, FEs usually drop when multiple steps with more electrons are involved in the reaction system. For example, CH$_4$, an 8-electron transfer product, needs a complex multiple proton-coupled electron transfer (PCET) process, which has lower selectivity for CO$_2$-to-CH$_4$ electro-reduction.[112,148] At this stage, the reported FEs for CH$_4$ can reach 92% on [Cu$_4$ZnCl$_4$(btdd)$_3$] (Cu$_4$-MFU-4l, H$_2$btdd = bis(1H-1,2,3-triazolo-[4,5-b],[4′,5′-i])dibenzo-[1,4]-dioxin) with trigonal pyramidal Cu($_1$)N$_3$ active sites.[121] C$_2$H$_4$ and C$_2$H$_5$OH, 12-electron transfer products, exhibit even more descending FEs (mostly below 60%) on MOF-based catalysts.[125–127,149]

Fig. 2 shows the possible intricate pathways of the CO$_2$RR classified using various reduction products. Variations in the final products – such as CO, CH$_4$, CH$_3$OH, C$_2$H$_4$, C$_2$H$_5$OH and so on can happen on electrocatalysts with the same or different

This journal is © The Royal Society of Chemistry 2024

J. Mater. Chem. A, 2024, **12**, 20578–20605 | **20581**

metal surfaces. For example, CO is a common product obtained from metals including Cu, Au, Ni, and Co during the electrocatalytic process.[150–153] Furthermore, differences in facets, sizes, and oxidation states of Cu can lead to various products [154–156] such as CO, CH_3OH and C_2H_4. Another example is formate, which is mostly produced on Bi and sometimes on In and Sb catalysts.[98,110,157] Here, the possible reaction pathways are categorized using various reduction products, as shown in Fig. 2. In the CO_2RR, *H, *CO, and *COOH (* denotes the surface-bond site) are typically key intermediates[158] that can further convert into various reaction intermediates. *H is involved in the PCET process in reduction pathways. *CO is a common intermediate for forming deeply reduced products. The electrophilicity of C and O in *CO dictates the subsequent reduction pathways. When the O atom in *CO first accepts a proton to generate *COH, it undergoes further reduction by accepting multiple protons and losing one water molecule to generate CH_4. On the other hand, when the C atom first accepts a proton to generate *CHO, the double bond between C and O opens to generate *CHOH, followed by further hydrogenation on C to produce methanol. Similar cases are also applied for *COOH and *HCOO. In terms of the *COOH intermediate, it is formed by transferring protons to O atoms of CO_2, followed by removing one water molecule to generate *CO. As for *HCOO, it is formed by transferring protons to the C atom of CO_2, followed by further hydrogenation to produce formate.

3. Electrochemical measurements and performance assessments

Evaluating the performance of electrocatalysts is crucial and is typically conducted using an electrochemical three-electrode system. Commonly employed testing techniques, including chronoamperometry/chronovoltammetry, linear sweep voltammetry (LSV), and electrochemical impedance spectroscopy (EIS) are utilized to determine parameters such as Faraday efficiency (FE), current density (J), overpotential (η), Tafel slope (b), turnover frequency (TOF), electrochemical surface area (ECSA) and stability. The key electrochemical characterization methods and evaluation parameters for electrocatalysts are summarized below.

3.1 Electrochemical measurements

3.1.1 Chronoamperometry/chronovoltammetry. Chronoamperometry is an electrochemical analysis technique that involves applying a constant potential step to the working electrode of an electrochemical system and tracking the current response over time. On the other hand, chronovoltammetry applies a rapidly increasing pulse current to the working electrode of an electrolytic cell, measuring the voltage between the working electrode and the reference electrode as a function of time. Both techniques are commonly used methods for the performance evaluation of the CO_2RR, from which faradaic efficiency, (partial) current density, and stability can be obtained.

3.1.2 Linear sweep voltammetry (LSV). LSV involves applying a linearly changing scanning potential and recording the corresponding current. The LSV curve is essentially half of a CV curve. In a reversible reaction, the peak current increases with the number of electrons gained or lost and the reaction area. The scanning speed directly affects the thickness of the diffusion layer. Higher scanning speed results in a thinner diffusion layer, greater potential gradient, and greater current. Therefore, the scanning speed needs to be controlled during testing. Additionally, an LSV can also be transformed to obtain a Tafel plot, providing insights into the reaction mechanism.

3.1.3 Electrochemical impedance spectroscopy (EIS). EIS entails the application of a small amplitude alternating current potential wave with varying frequencies to an electrochemical system. By measuring the ratio of the alternating current potential to the current signal *versus* the sine wave frequency (ω), or the change in the impedance phase angle (Φ) with frequency, EIS offers valuable information about the system. As conductivity of MOFs is still one of the challenges to be addressed when applied as electrocatalysts for the CO_2RR, EIS can be an effective method to evaluate the feasibility of MOF catalysts from the evaluation of resistance.

3.2 Performance assessments

3.2.1 Faradaic efficiency (FE). FE is a crucial parameter for evaluating the selectivity of electrocatalysts. It is defined as the percentage of charge consumed to generate the desired products in the total charge during the CO_2RR process,[159] which can be expressed as:

$$FE = \frac{\alpha n F}{Q} \times 100\% \tag{18}$$

where α is the molar amount of the desired product; n is the number of electrons transferred to obtain a certain product; F is the Faraday constant ($96\,485\,C\,mol^{-1}$); Q is the total charge consumed in the entire reaction.

3.2.2 Current density (J). J reflects the reaction efficiency of the electrochemical conversion, usually including the total current density (J_t) and partial current density (J_p). J_t can be calculated by dividing the total current by the geometric area of the working electrode (S). J_p is obtained by multiplying the FE with J_t, which corresponds to the production rates of a certain product:

$$J_t = J/S \tag{19}$$

$$J_p = FE \times J_t \tag{20}$$

3.2.3 Overpotential (η). η is a criterion for assessing the activity of electrocatalysts, representing the additional driving force required to overcome the reaction energy barrier and facilitate the redox reaction. It can be described as the difference between the standard thermodynamic reaction potential (E^0) and the practical electrode potential (E_{cat}), [160] as shown in the following equation:

20582 | *J. Mater. Chem. A*, 2024, **12**, 20578–20605

This journal is © The Royal Society of Chemistry 2024

$$\eta = E^0 - E_{cat} \tag{21}$$

3.2.4 Tafel slope (*b*). The Tafel slope reflects the kinetics of electrocatalysts for the CO_2RR. A smaller Tafel slope indicates faster kinetics and superior performance. The Tafel slope is related to the overpotential, which can be calculated according to the following equation:

$$\eta = b \times \log j_p + a \tag{22}$$

Here, η, b, j_p, and a represent the overpotential, Tafel slope, partial current density of a certain product, and a constant. When the Tafel slope is close to 118 mV dec^{-1} or 59 mV dec^{-1}, the reaction rate is determined by the CO_2 activation or the *COOH intermediate formation.[161]

3.2.5 Turnover frequency (TOF). TOF, defined as the total number of molecules that undergo a reaction per second per active site, usually reflects the intrinsic activity of an individual active site of catalysts.[162] TOF can be calculated using:

$$TOF = (J_t \times FE)/(nFn_a) \tag{23}$$

where J_t, FE, n, F and n_a represent the total current density, Faraday efficiency, the electron transfer number for a desired product, the Faraday constant (96 485C mol^{-1}) and the number of active sites on the electrode.

3.2.6 Electrochemical surface area (ECSA). The total current density, calculated with respect to the geometric area of the electrode, is indicative of the catalyst loading and specific surface area, a metric that can be normalized through ECSA. A greater ECSA value typically correlates with enhanced CO_2 reduction performance. The ECSA can be approximated using the double-layer capacitance (C_{dl}):

$$ECSA = C_{dl}/C_s \tag{24}$$

in which C_{dl} is obtained by measuring the current with different scanning rates at a nonfaraday current area and C_s is the specific capacitance of smooth surface samples.

3.2.7 Stability. Stability is a crucial evaluation criterion for practical application. Long-term stability can be evaluated by chronoamperometry and chronovoltammetry. Greater stability is denoted by minimal fluctuation during testing. At this stage, stability remains one of the bottlenecks of MOF electrocatalysts, which will be discussed later in this review.

4. Insights into catalyst design: why MOFs?

As discussed, there are so many possible pathways toward various products that occur during the CO_2RR. Developing high-selectivity electrocatalysts is still a great challenge in this field. A deep insight into the structure-reactivity correlations is thus highly demanded to provide principles for designing high-performance electrocatalysts. MOFs as a type of material with well-defined structures are suitable to be studied as model catalysts for the fundamental study to unravel the true active sites for the CO_2RR. Furthermore, given the nearly infinite number of potential metal nodes and coordinating organic linker combinations, MOFs display a wide range of chemical and structural variability, which makes them attractive catalyst candidates with tailorable properties for the CO_2RR. However, low conductivity and stability remain the bottlenecks of MOFs, which restricts their application in the electrochemical CO_2RR.[84] In the past few decades, it has been demonstrated that electrocatalytic performance can be improved by regulating atomically dispersed metal catalytic sites and the coordination environment around them in MOFs.[163–166] In this section, we focus on the molecular engineering of MOFs for enhanced CO_2RR activity and selectivity toward desired products mainly based on the roles of metal nodes and coordinating organic ligands.

4.1 Regulation of metal nodes

MOFs with a periodic network structure possess uniformity and nearly 100% atomically dispersed sites, whose porous structure facilitates the adsorption and transport of CO_2.[167] The metal nodes of MOFs coordinated with organic ligands serve as active sites to speed up reaction rates, selectively transforming CO_2 into the desired products in a certain pathway. A family of typical two-dimensional (2D) flat MOFs [$TM_3(HAB)_2$, TM = Fe, Co, Ni and Cu; HAB = hexaaminobenzene] was reported by Tang *et al.*[168] in which the TM bonded with four N atoms. According to the calculations using DFT methods combined with the computational hydrogen electrode (CHE) model, $Fe_3(HAB)_2$ exhibited the strongest adsorption of *COOH and *H among these compounds, leading to the highest activity toward CO_2 production. The reaction pathway was proven to be a proton-assisted mechanism through a pathway of "$CO_2 \rightarrow$ *COOH $\rightarrow$ *CO $\rightarrow$ *CHO $\rightarrow$ *CHOH $\rightarrow$ *CH$_2$OH $\rightarrow$ CH$_3$OH". Thus, $Fe_3(HAB)_2$ was identified as a promising material catalyzing CO_2 to CH_3OH *via* the "RWGS (reverse water gas shift) + CO-hydro (CO hydrogenation)" process. Similarly, Cui *et al.*[169] also performed the calculation of conductive [$TM_3(HAB)_2$, TM = Fe, Co, Ni, Cu, and Mo]. Fe-, Co- and Ni-based MOFs presented weak adsorption of CO_2, while Cu-based MOFs exhibited strong adsorption energies of CO_2 and H_2O, with a higher interaction with H_2O than with CO_2. In terms of Mo-based MOFs, they were identified as favorable candidates for adsorbing more CO_2 molecules than H_2O. The different charge density of CO_2 adsorbed on Mo-based MOFs displayed a distorted CO_2 molecule, indicating the good activation and selectivity of CO_2.

M_3(hexaiminotriphenylene)$_2$, one type of conductive MOF, known as $M_3(HITP)_2$ (M = Ni^{2+}, Cu^{2+}, HITP = hexaimino-triphenylene), has also been applied to the CO_2RR. The selectivity of $M_3(HITP)_2$ for the CO_2RR can be regulated by varying the metal nodes. A series of $M_3(HITP)_2$ (M = Fe, Co, Ni, Ru, Rh, and Pd) samples were investigated for the CO_2RR using DFT calculations. However, only $Co_3(HITP)_2$ and $Rh_3(HITP)_2$ exhibited superior selectivity toward CH_3OH formation.[170] This was attributed to the strong chemical activity toward *COOH species and high *CO adsorption strength, which indicated that

This journal is © The Royal Society of Chemistry 2024

J. Mater. Chem. A, 2024, **12**, 20578–20605 | **20583**

the adsorbed CO_2 molecule can be activated and further reduced without desorption. $Co_3(HITP)_2$ and $Rh_3(HITP)_2$ with respective overpotentials of 0.67 V and 0.46 V exhibited superior catalytic activity. Similarly, the CO_2RR performance of bis(iminothiolato)metals (marked as TMIT, TM = Mn, Fe, Co, Ni, Cu, Ru, Rh, and Pd, IT = $C_6S_3N_3H_3$) can also be affected by the metal nodes as simulated by spin-polarized calculations.[171] All these catalysts catalyzed CO_2 to produce HCOOH except that RuIT and RhIT only catalyzed CO production. This was because the strong adsorption of CO on the RuIT and RhIT catalyst surfaces poisoned the catalysts. π-conjugated metal bis(dithiolene) complex nanosheets ($M_3C_{12}S_{12}$, M = Fe, Co, Ni, Ru, Rh, and Pd)[172] within spin-polarized frameworks were another typical type of MOF. However, $Fe_3C_{12}S_{12}$, $Co_3C_{12}S_{12}$, $Ni_3C_{12}S_{12}$, and $Pd_3C_{12}S_{12}$ sheets exhibited weak chemical activity toward *COOH and *HCOO intermediates due to their high free energies ($\Delta G > 0.74$ eV), and thus these four catalysts were not considered to suit CO_2RR applications. CO desorption and further hydrogenation on $Ru_3C_{12}S_{12}$ were indicated to be thermodynamically disadvantageous, while $Rh_3C_{12}S_{12}$ was suggested to be a potential catalyst for the CO_2RR due to its low free energy barrier and thus thermodynamic advantages. Additionally, a porous 2D graphene-like sheet $M_3(HHTQ)_2$ (M = Cu, Ni) was also constructed from 2,3,7,8,12,13-hexahydroxytricycloquinazoline with Ni^{2+} and Cu^{2+} (ref. 138) (Fig. 3a). $Cu_3(HHTQ)_2$ showed stronger CO_2 adsorption than $Ni_3(HHTQ)_2$ and higher FE_{CH_3OH} up to 53.6% at an overpotential of −0.4 V.

Doping diverse metal ions into MOFs is an attractive synthetic strategy to enhance the performance of the CO_2RR due to the unique characteristics introduced by additional metal nodes, which may have synergistic effects.[67,68,173–175] For instance, Cho et al.[69] reported a series of zeolite-imidazolate frameworks (ZIF-8) containing Ni^{2+}, Fe^{2+}, and Cu^{2+} (Fig. 3b). $Cu_{0.5}Zn_{0.5}$/ZIF-8 achieved a higher FE of 88.5% for CO than pristine ZIF-8 (43.7%), $Ni_{0.1}Zn_{0.9}$/ZIF-8 (34.7%) and $Fe_{0.3}Zn_{0.7}$/ZIF-8 (48.8%). This was because the doped Cu affected the electronic structures of electron-rich sp^2 C sites via a local effect between the zinc-nitrogen (Zn–N_4) and copper-nitrogen (Cu–N_4) sites, which facilitated *COOH adsorption and promoted the reduction reaction. Iqbal et al.[50] reported bimetallic Ni and Fe in MOFs (MOF Ni–Fe). The incorporated combination of Ni and Fe metal centers increased the active surface area and active sites for the adsorption of intermediates, promoting the CO_2RR process. As a result, the Ni and Fe bimetallic centers lowered the kinetic energy barrier, which achieved a FE_{CO} of 98.2%, superior to single metal MOF-Ni (74.3%) and MOF-Fe (62.6%).

The construction of heteronuclear metal pair sites in MOFs can be used to regulate the kinetic energy barrier of intermediate formation for enhanced CO_2RR performance. For instance, Zhong et al.[68] developed a layer-stacked 2D conjugated MOF (PcCu-O_8-Zn) with CuN₄ (copper-phthalocyanine) and ZnO₄ (zinc-bis(dihydroxy)) to promote CO_2 into syngas (CO and H_2). The molar ratio of H_2/CO (1 : 7 to 4 : 1) was tuned by varying metal nodes (Cu and Zn) and applied potentials. ZnO₄ showed high catalytic activity in converting CO_2 to CO, while the CuN₄ unit promoted the HER process. Synergistic catalytic effects were achieved using ZnO₄ and CuN₄ metal nodes. Another

example was the integration of 2,3,9,10,16,17,23,24-octasubstituted metallophthalocyanine (MPc-XH, M = Co and Ni, X = N and O) into conductive MOFs as electrocatalysts for the CO_2RR.[67] The activity and selectivity were tailored by the selection of metal nodes of MPcs and further adjustment of heteroatomic linkages. CoPc–Cu–O achieved an FE_{CO} of 79% and a current density of −9.5 mA cm^{-2}. This is because CoPc-based and O-linked MOFs lowered the activation energies toward *COOH formation, resulting in higher activity and selectivity. CuSn-HAB,[143] a conductive 2D π-conjugated MOF with hexaaminobenzene (HAB) ligands and planar Cu–N_4 nodes, had a pair of SnN_2O_2 and CuN_4 sites bridged by μ-N atoms and demonstrated an FE of 56% toward CH_3CH_2OH formation. Further investigations revealed that the SnN_2O_2 site exhibited a higher affinity for O atoms compared with the copper site, playing an important role in promoting the formation of the *OCH_2 intermediate. Therefore, the dual sites were more thermodynamically favorable for the C–C coupling between *CO and *OCH_2. In addition, Cu–Ni dual-metal sites also showed similar synergistic effects for high selectivity.[139] The UiO-66(Hf) matrix helped stabilize the single atoms and facilitating ionizing radiation conversion, while atomic Cu–Ni dual-metal sites contributed to high CH_3OH selectivity. Under radiation conditions, CuNi SAs/UiO-66(Hf) realized a selectivity of ∼98% for CH_3OH and an energy efficiency of ∼1.5×10^{-7} mol J^{-1}. The spectral data and calculations showed that three C_1 intermediate adsorption states may occur at the Cu site and the final two at the Ni site, leading to selective CH_3OH formation.

Similarly, the same nuclear metal pair also showed synergetic effects on the promoted performance of the CO_2RR. (2,3,9,10,16,17,23,24-octahydroxyphthalo-cyaninato) copper(II) (PcCu–$(OH)_8$) ligands and the CuO_4 nodes were used to construct a MOF catalyst (PcCu–Cu–O).[127] PcCu–Cu–O with dual active sites exhibited high performance to convert CO_2 to C_2H_4 with a FE of 50% and a current density of 7.3 mA cm^{-2}. It was also found that dimer-copper catalysts $Cu_2^{II}[BH(mim)_3]_2Cl_2$ (BIF-102, BIF = boron imidazolate frameworks, mim = 2-methylimidazole) with Cl$^-$ bridged dimer copper (Cu_2) units delivered high activity and selectivity for C_2H_4 (ref. 122) (Fig. 3c). The enhanced performance was due to the enriched charge around the dual Cu centers in $Cu_2^{II}[BH(mim)_3]_2Cl_2$ which performed as regulators for varying the energy barriers and afforded distinct reaction pathways. Therefore, $Cu_2^{II}[BH(mim)_3]_2Cl_2$ BIF-102NSs (NS = nanosheet) exhibited improved FE of C_2H_4 (11.3%), superior to iso-reticular BIF-103 ($Cu_2^{II}[BH(mim)_3]_2(-HCOO)_2$, 7.15%) and single-metal BIF-104 ($Cu^{II}[BH(mim)_3](BA)$, 3.55%).

MOFs containing multi-metallic redox-active secondary building units (SBUs) have also been reported to be good candidates for high-performing electrocatalysts. Huang et al. reported an alkali-resisting MOF (Cu_1Ni-1,4-benzenedipyrazolate, Cu_1Ni-BDP) featuring pyrazolate-stabilized asymmetric Ni/Cu clustersites for the CO_2RR.[176] The unique Ni–Cu hybrid sites, characterized by an asymmetric electronic structure, orbital interaction and close distance (2.8 Å), synergistically catalyzed the conversion of CO_2 to C_2H_4. In an alkaline environment (1.0 M KOH), Cu_1Ni-BDP exhibited
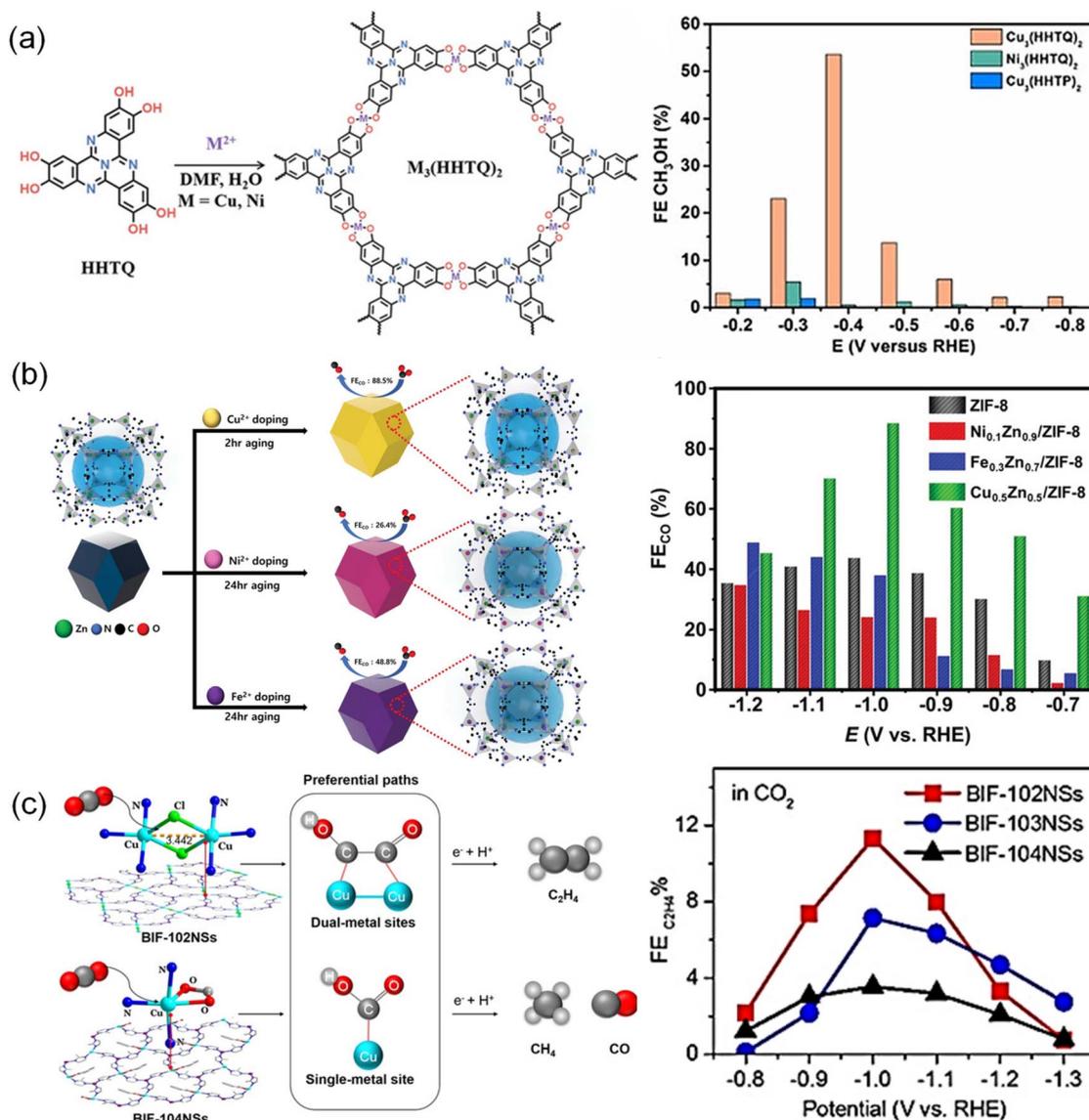
20584 | J. Mater. Chem. A, 2024, **12**, 20578–20605

This journal is © The Royal Society of Chemistry 2024

Fig. 3 (a) Schematic synthesis of $M_3(HHTQ)_2$ (M = Cu, Ni) and FE of CH_3OH.[138] Copyright 2021, Wiley-VCH. (b) Schematic synthetic strategy of the M_xZn_y/ZIF-8 catalyst and FE of CO.[69] Copyright 2023, Wiley-VCH. (c) Coordination environment and reaction pathways for BIF-102NSs and BIF-104NSs as well as FE of C_2H_4.[122] Copyright 2021, Wiley-VCH.

a notable C_2H_4 selectivity, yielding an FE of 52.7% and a partial current density of 278 mA cm^{-2} at −1.3 V. Moreover, only a 4.5% decrease in FE was observed after 25 h of electrolysis. *Operando* analyses and theoretical calculations indicated that the asymmetric Ni/Cu sites effectively reduced the energy barrier associated with the *COH–COH intermediate, the rate-limiting step in CO_2 reduction to C_2H_4. MOFs containing heterobimetallic cluster sites offer the potential for synergistic catalysis or tandem catalysis toward C_{2+} production. Similarly, two-dimensional $Ru_2(OAc)_4Ni(CN)_4$, featuring Ru and Ni bimetallic metal sites was reported to exhibit high activity and selectivity for 1-C_4H_8 production.[177] At room temperature, it achieved a production rate of 1.3 mol g_{cat}^{-1} h^{-1} and conversion efficiency of 97%. Trinuclear clusters within MOFs have also been proven to be effective in the electrochemical CO_2RR to

produce value-added products. Huang *et al.*[130] reported a low-cost metal-azolate framework $[Cu_3(\mu_3\text{-}OH)(\mu_3\text{-}trz)_3(OH)_2(H_2\text{-}O)_4](Cutrz)$ constructed from 1H,1,2,4-triazole (Htrz) organic ligands and $Cu_2SO_4 \cdot 5H_2O$ salts. The Cutrz MOF with trinuclear clusters as active sites displayed a high FE of 50% for selective electroreduction of CO_2 to C_2H_4. The trinuclear cluster $\{Cu_3(\mu_3\text{-}OH)(\mu_3\text{-}trz)_3\}^{2+}$ enabled the simultaneous adsorption of three *CO intermediates on its surface, positioning closely at only 3.3 Å apart. This close proximity led to higher *CO coverage and facilitated C–C dimerization coupling with a reduced energy barrier. By tailoring the size of the monodispersed CuTrz, the catalyst's performance was further enhanced to 55.4%.[130] CuTrz particles with an average size of 109 nm showed superior activity compared to their larger counterparts. Extensive characterization studies revealed that the remarkable selectivity was
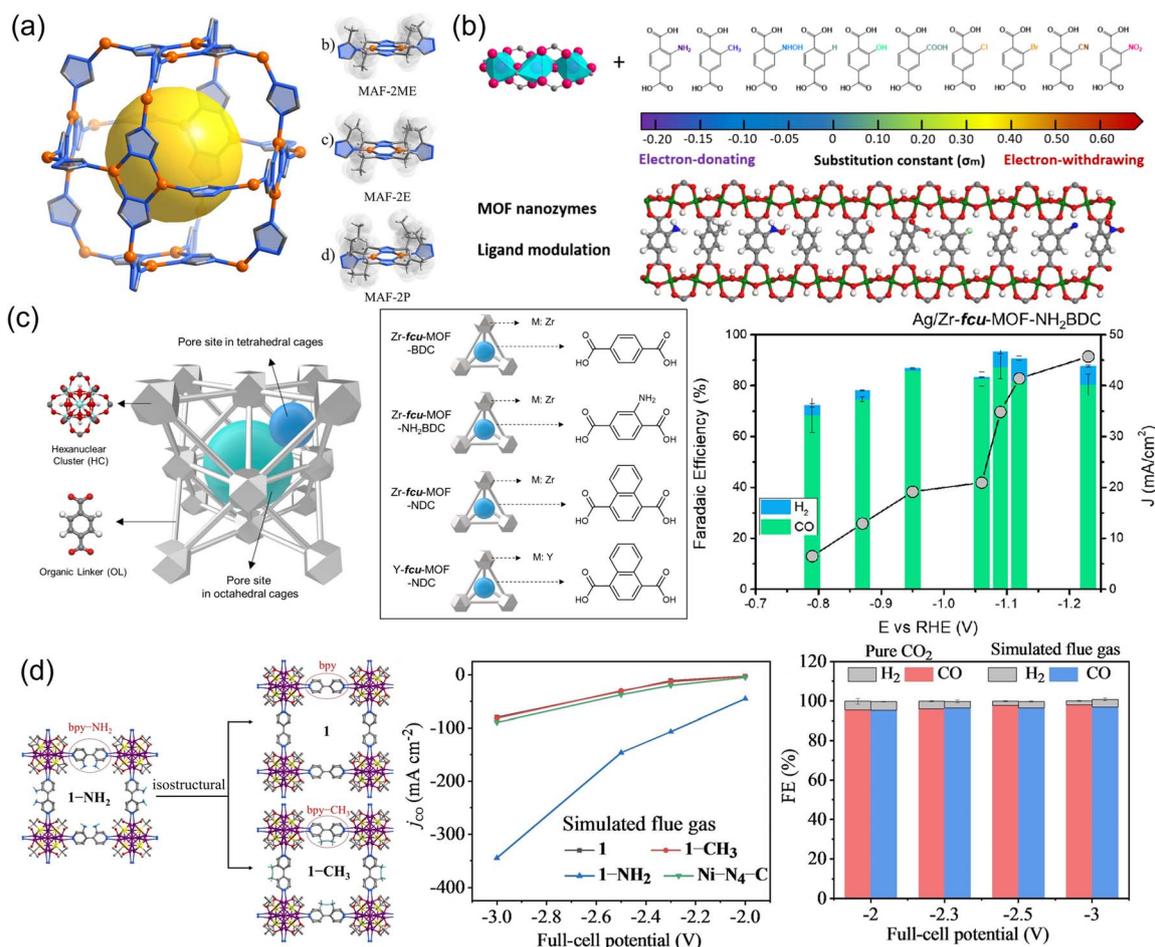
This journal is © The Royal Society of Chemistry 2024

J. Mater. Chem. A, 2024, **12**, 20578–20605 | **20585**

Fig. 4 (a) Crystal structures and local coordination environments of MAF-2 analogs.[49] Copyright 2022, Wiley-VCH. (b) Ten possible ligand-decorated 1,4-benzenedicarboxylic acid linkers with their substituent constant values.[183] Copyright 2023, American Chemical Society. (c) MOF design strategies based on the Zr-*fcu*-MOF-BDC MOF and FE of CO for Ag/Zr-*fcu*-MOF-NH₂BDC.[77] Copyright 2020, American Chemical Society. (d) Schematic of 1, 1-CH₃ and 1-NH₂, j_{CO} of 1, 1-CH₃, 1-NH₂ and Ni−N₄−C catalysts under simulated flue gas and FE$_{CO}$ for 1-NH₂ in CO₂ and simulated flue gas.[82] Copyright 2023, Wiley-VCH.

attributed to the uniform small size of CuTrz and the presence of abundant grain boundaries.

4.2 Modulation of surrounding organic ligands

Though metal nodes of MOFs play a significant role in determining the activity and selectivity of the CO₂RR, it is important to note that the same type of metal nodes in different MOFs may result in different pathways toward different carbon products. The variation in catalytic behaviors may be attributed to differences in the electronic properties of metal nodes in different types of MOFs, including their oxidation state[178,179] and electron density,[180] which are significantly influenced by the metal coordination geometry and ligand environment. In this section, the important contribution of the ligands surrounding the metal nodes of MOFs to the CO₂RR is discussed. In general, organic ligands in MOFs play an essential role in regulating specific sizes, geometries, and symmetries.[181] It is considered that MOFs can achieve outstanding catalytic activity and stability for the CO₂RR through rational design of building

blocks with specific functional groups, side structures and modification with small molecules.[78,182] The regulation strategy generally includes the modulation of side groups and the body structure of organic ligands.

By changing the size of ligand side groups, Cu(I) triazolate frameworks (MAF-2ME, MAF-2E, and MAF-2P) were tailored to realize high-efficiency conversion of CO₂ to C₂H₄/CH₄[53] (Fig. 4a). The C₂H₄/CH₄ selectivity ratio can be tuned and inversed from 11.8 : 1 to 1 : 2.6 with selectivity up to 51% (C₂H₄), 56% (CH₄), and 77% (hydrocarbon), respectively. Computational simulations showed that the geometry structure of Cu(I) changed from triangular to tetrahedral due to the change of ligand side groups, with two adjacent Cu(I) cooperating for C−C coupling to form C₂H₄. Recently, Mao et al.[183] synthesized Cu-based MOFs with an optimal Cu−Cu distance, named MIL-53 (Cu) (MIL = Materials of Institute Lavoisier) (Fig. 4b). Ten different ligand side groups from electron-donating groups (NH₂, CH₃, NHOH, OH, and H) to electron-withdrawing groups (COOH, Cl, Br, CN, and NO₂) were chosen to decorate the organic ligand in MIL-53 (Cu) to modulate the Cu−Cu distance

20586 | *J. Mater. Chem. A*, 2024, **12**, 20578−20605

This journal is © The Royal Society of Chemistry 2024

and charge of Cu. COOH-ligand-decorated MIL-53 (Cu) was located at the top of the volcano plot and exhibited the highest catalytic activity and selectivity toward CH_3CH_2OH production. COOH-ligand-decorated MIL-53 (Cu) exhibited high catalytic performance with a FE of 55.5%, which was superior to that of the Cu electrode (35.7% at −1.05 V *vs.* RHE). Similarly, Nam *et al.*[77] added side groups of −NH_2 in a face-centered cubic (***fcu***) MOF to strengthen the adsorption capacity of CO_2 (Fig. 4c). As a result, FE_{CO} increased and FE_{H_2} decreased on Ag/Zr-***fcu***-MOF-NDC (H_2BDC: 1,4-benzenedicarboxylic acid) compared to Ag/Zr-***fcu***-MOF-BDC and Ag/Zr-***fcu***-MOF-NH_2BDC. They also explored the role of the body structure of ligands in modifying the binding modes of *CO intermediates, which played a pivotal role in product selectivity. The high CO_{bridge} population in Ag/Zr-***fcu***-MOF-NDC (H_2NDC: 1,4-naphthalenedicarboxylic acid) was modulated for enhanced CO selectivity. Aromatic amine groups were also coupled into a silver chalcogenolate cluster-based MOF ($Ag_{12}(S^tBu)_8(CF_3COO)_4(bpy-NH_2)_4$, denoted as 1-$NH_2$, aka-$Ag_{12}$bpy-$NH_2$, bpy-$NH_2$ = 3-amino-4,4′-bipyridine) to capture CO_2 molecules in a simulated flue gas and served as CO_2 catalytic sites[82] (Fig. 4d). The 1-NH_2 MOF could catalyze the adsorbed CO_2 into CO with an ultra-high CO_2 conversion of 60% and a FF_{CO} of 96% due to the introduction of the aromatic amine groups, better than $[Ag_{12}(S^tBu)_8(CF_3COO)_4(bpy)_4]$ (bpy: 4,4′-bipyridine, 1, aka Ag_{12}bpy) and $[Ag_{12}(S^tBu)_8(CF_3COO)_4(bpy-CH_3)_4]$ (bpy-CH_3: 3-methyl-4,4-bipyridine, 1-CH_3, aka Ag_{12}bpy-CH_3).

Modifying the body structure of organic ligands has also been reported as an effective strategy to enhance CO_2RR performance. For instance, changing the ligand body structure of ligand linkers in Cu naphthalenedicarboxylate (Cu-UNDC) and Cu benzenedicarboxylate (Cu-UBDC) can regulate the MOF structure and electronic environment of Cu centers, thus changing the selectivity toward C_2 products[184] (Fig. 5a). The two catalysts showed different FEs for C_2 products. FEs for Cu-UBDC were 13.2% in the dark and 26.2% in the light. FEs for Cu-UNDC were 24.3% in the dark and 21.8% in the light. Moreover, in-built heteroatoms within the molecular structure of organic ligands lead to significant variations in the electrocatalytic CO_2RR. Liu *et al.*[118] designed and synthesized a 2D conjugated Cu MOF (HATNA-Cu-MOF) by coordination of an electron-deficient N-containing conjugated molecule HATNA-6OH (hex-aazatrinaphthylene) and Cu(NO_3)$_2$. The symmetric aromatic heterocycle of HATNA-6OH with 6 hydroxyl groups makes it selectively coordinate with Cu^{2+} in a 2D framework, with three phenanthroline units as additional sites for guest binding. The
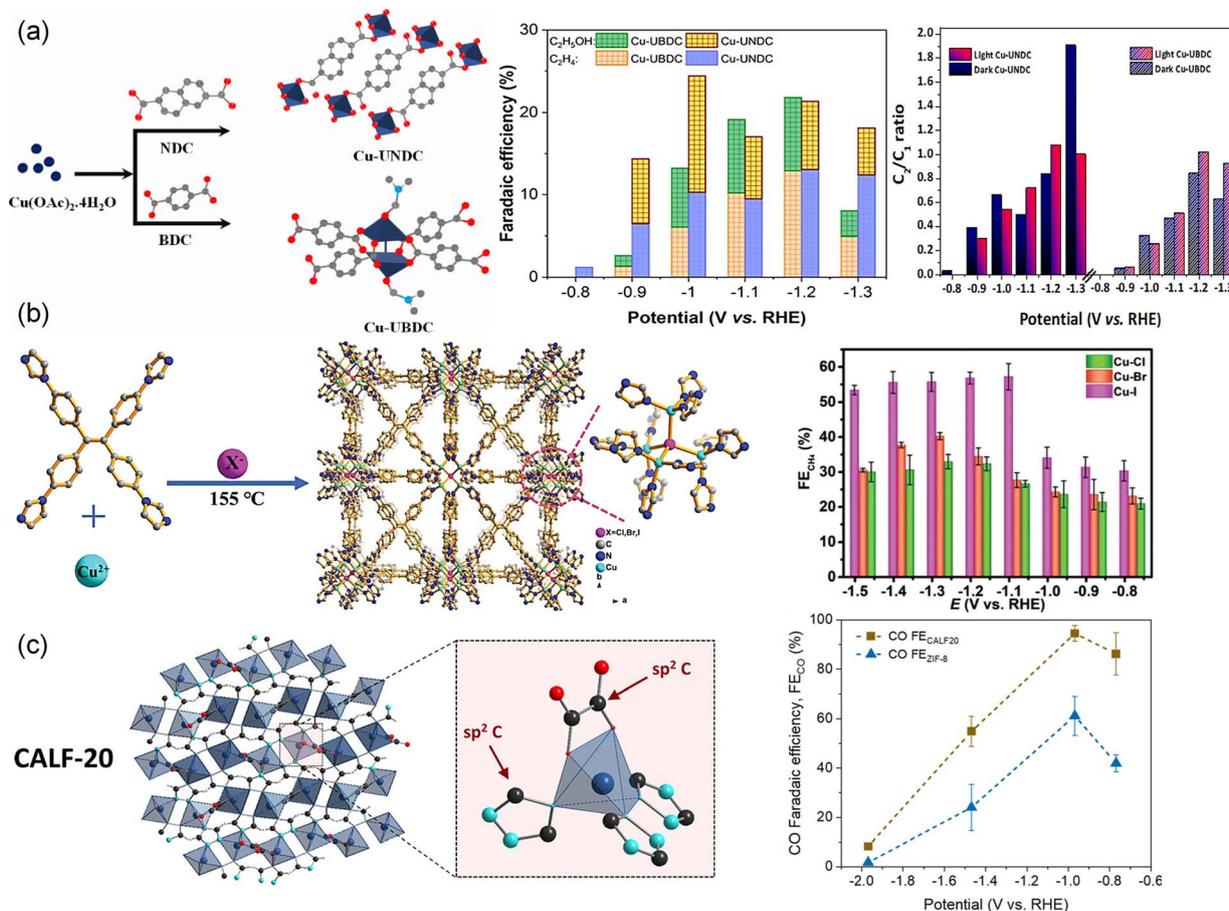

Fig. 5   (a) Schematic, FE toward C_2 products and the C_2/C_1 ratio of Cu-UNDC and Cu-UBDC in CO_2-saturated 0.1 M KHCO$_3$.[184] Copyright 2023, American Chemical Society. (b) Schematic illustration of the structure and FE_{CH_4} of Cu-X (X = Cl, Br and I).[58] Copyright 2022, Wiley-VCH. (c) Schematic illustration of the crystal structure of CALF20 and FE_{CO} of ZIF-8 and CALF20.[78] Copyright 2021, American Chemical Society.

This journal is © The Royal Society of Chemistry 2024

J. Mater. Chem. A, 2024, **12**, 20578–20605 | **20587**

synergistic effects of HATNA and copper catecholate nodes enabled the conjugated HATNA-Cu-MOF to selectively convert CO_2 to CH_4 with an FE of 78% at −1.5 V. The tailoring of ligands can adjust both the coordination microenvironment of metal nodes and geometry structure of MOFs, thereby affecting their electronic structure and interaction with intermediates. Recently, a series of Cu(I)-based MOFs ([$Cu_4X(TIPE)_3$]·3X, [X = Cl, Br, I, TIPE = 1,1,2,2-tetrakis(4-(imidazole-1-yl)phenyl) ethene]) with different coordination microenvironments (Cu–Cl, Cu–Br, and Cu–I) were synthesized by Sun *et al.*[58] (Fig. 5b). With the increasing radius of halogen atoms from Cl to I, the CO_2 adsorption increased and the d-band center of Cu positively shifted to the Fermi level, resulting in enhanced selectivity of CO_2 to CH_4. The shifted d-band center reduced the formation energies of *CH_2O and *CH_3O species from Cl to I and thus enhanced the electrocatalytic activity. The MOF with a Cu_4I cluster (X = Cl, Br and I) gave a partial current density of 60.7 mA cm^{-2} and FE of 57.2% for CH_4 production at −1.08 V compared with Cu–Cl (32.9%) and Cu–Br (40.2%) at −1.28 V. Al-Attas *et al.*[78] explored Zn-based MOFs with two different azolate functional ligands, 1,2,4-triazole (Calgary Framework 20, CALF20, [$Zn_2(Tz)_2Ox$]) and 2-methylimidazole (zeolitic imidazolate framework-8, ZIF-8, [$Zn(MeIm)_2$]) for the CO_2RR (Fig. 5c). CALF20 showed higher FE for CO (94.5%) compared to ZIF-8 (61.1%). The sp^2 carbon atoms in 1,2,4-triazole ligands coordinated with the Zn(II) centers were claimed as the active sites for the CO_2RR, as 3d orbitals of Zn(II) centers were fully occupied. In addition, *ab initio* investigation showed that the N-sp^2 C adsorption site was the most favorable adsorption sites in CALF20 and ZIF-8. The 1,2,4-triazole ligand in CALF20 with more electrons induced in the adjacent active sites enhanced the charge transfer and facilitated *COOH formation, promoting CO production with high current density and FE.

The researchers further assembled CALF20 into a gas diffusion electrode and realized a 95% FE for converting N_2-diluted CO_2 streams to CO.[185]

4.3 Post-modification

As a matter of fact, incorporation of functional modules into MOFs for enhancing CO_2RR performance can be realized not only through direct synthesis but also through post-modification. Therefore, doping extraneous ligands in MOFs is one of the most effective strategies. For example, ZIFs, a subclass of MOFs assembled using metal nodes and imidazole ligands, exhibited excellent thermal and chemical stability with various topologies.[66] Active sites were considered to be the imidazolate ligands coordinated with the Zn(II) nodes in ZIFs with ZIF-8 showing the highest FE_{CO} of 81.0% and a current density of 12.8 mA cm^{-2}.[66] Later, Dou *et al.*[71] developed a ligand doping strategy by introducing 1,10-phenanthroline into ZIF-8 using a post-treatment process. The conjugated structure of 1,10-phenanthroline might benefit from electron delocalization and increased the electron density around nitrogen, thereby facilitating π electron transfer and enhancing σ electron donation between nitrogen and the metal.[186] In this study, 1,10-phenanthroline acted as an electron donor, induced the adjacent sp^2 C atoms in imidazolate and thus strengthened the ability of *COOH formation, delivering a high FE of 90.57%. Also, metallocene[84] had a similar impact on the improvement of electron conductivity and electron-donating ability. Using the chemical vapor deposition method, metallocene was implanted in MOF-545-Co. The as-prepared $CoCp_2$@MOF-545-Co selectively converted CO_2 to CO with an FE of 97% due to its strong binding interaction, which reduced the adsorption energy of CO_2. This method can be applied universally to other materials. For instance, diphenyl sulfide immobilized onto graphene
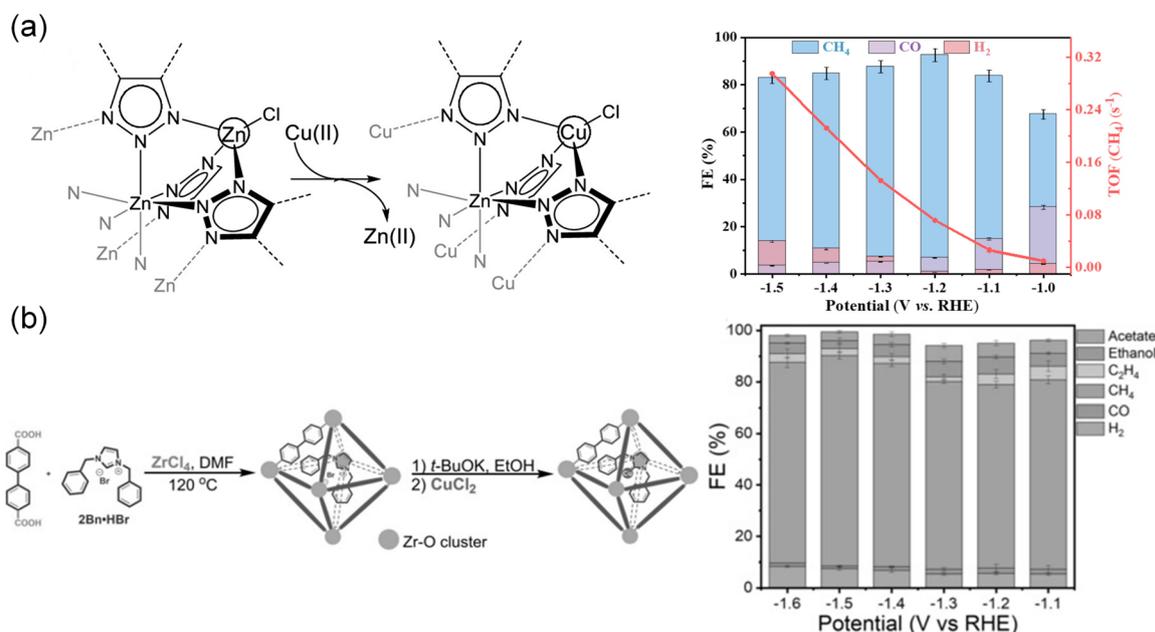

Fig. 6 (a) Schematic of the metal transformation process, and FE_{CH_4} and TOF of Cu_4^{II}-MFU-4*l*.[121] Copyright 2021, American Chemical Society. (b) Schematic synthesis route and FE of 2Bn-Cu@UiO-67.[120] Copyright 2021, Wiley-VCH.

20588 | *J. Mater. Chem. A*, 2024, **12**, 20578–20605

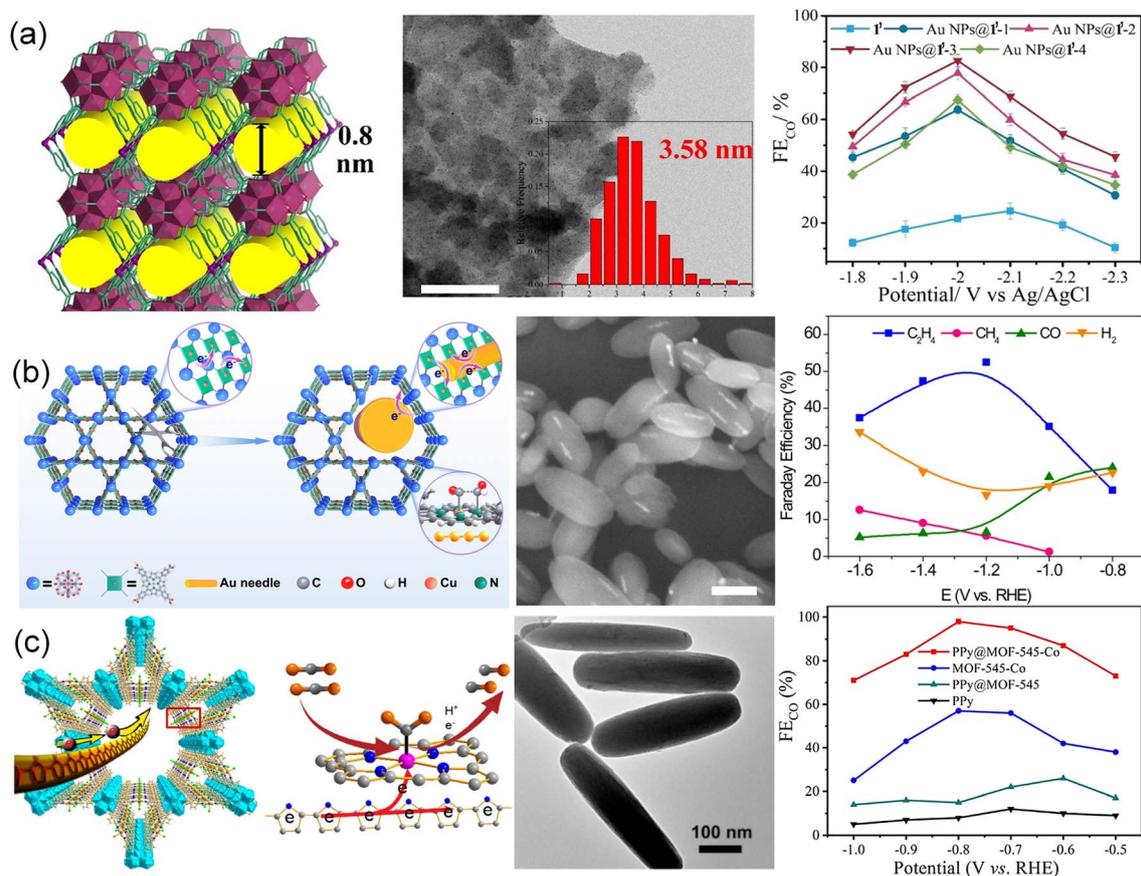This journal is © The Royal Society of Chemistry 2024

Fig. 7 (a) Three-dimensional framework of **1**′, TEM image of Au-NPs@**1**′-3 and FE_{CO} of Au NPs@**1**′-x (x = 1, 2, 3, and 4).[51] Copyright 2022, Wiley-VCH. (b) Schematic illustration, the SEM image and FE for different products of the AuNN@PCN-222(Cu) catalyst.[188] Copyright 2022, Springer Nature. (c) Schematic illustration for the advantages of PPy in MOF-545-Co, the TEM image of PPy@MOF-545-Co and FE_{CO} of PPy@MOF-545-Co at different voltages.[189] Copyright 2021, American Chemical Society.

served as an axial ligand for tetraphenylporphyrin cobalt (PCo), while [PCo]*⁻ acted as active sites promoting CO_2 reduction.[187] The benzene rings of diphenyl sulfide stacked with graphene in a face-to-face manner, serving as a mediator for the electron transfer communication between PCo and graphene.

Doping extra metal elements in MOFs was an effective method to prepare high-efficiency MOF electrocatalysts. Recently, a new 2D Fe-based BIF-73-NS (BIF = boron imidazolate framework, NS = nanosheet) MOF was successfully synthesized through ultrasonication exfoliation of bulk BIF.[70] Benefiting from the functional –OH groups, Fe ions were anchored, and molecular-level Fe_2O_3 was formed in 2D BIF-73-NS. 2D BIF-73-NS with Fe_2O_3 fragments exhibited a high FE_{CO} of 88.6% at −1.8 V vs. Ag/AgCl. In addition, Zhu et al.[121] prepared Cu_4^{II}-MFU-4l by exchanging partial Zn(ɪɪ) ions in MFU-4l ([Zn_5-Cl_4(btdd)$_3$], H_2btdd = bis(1H-1,2,3-triazolo-[4,5-b], [4′,5′-i]) dibenzo-[1,4]-dioxin)) with Cu(ɪɪ) irons (Fig. 6a). In situ X-ray absorption spectroscopy (XAS) and infrared (IR) spectroscopy spectra revealed that $Cu(ɪ)N_3$ was in situ formed from Cu(ɪɪ) species, acting as an active site. $Cu(ɪ)N_3$ showed strong coordination ability and synergistic effects with adjacent aromatic hydrogen atoms, playing an important role in stabilizing the key intermediates and suppressing the competitive HER, thus

showing high electrocatalytic activity and selectivity for CH_4 formation (FE = 92%).

Additionally, an encapsulation strategy was also proposed to prepare MOF electrocatalysts with enhanced performance in the CO_2RR. Chen et al.[120] encapsulated N-heterocyclic carbene molecules (NHCs, 1,3-dibenzyl-1H-imidazole-3-ium bromide, 2Bn-HBr) into UiO-67 for their well-matched molecular size. Cu was added to the alkaline medium to synthesize 2Bn-Cu@UiO-67 (Fig. 6b). Due to the acidic C–H bond of the imidazole, NHCs with a lone pair of electrons tended to bond with the metal to generate a stable NHC-metal complex. 2Bn-Cu@UiO-67 achieved 81% FE of CH_4 and a high TOF of 16.3 s⁻¹. It was suggested that σ donation of NHC enhanced the surface electron density of Cu catalytic sites and optimized the adsorption of *CHO species.

A novel 3D framework **1**′ {[$Ni_3Zr_6(\mu_3$-O)$_4(\mu_3$-OH)$_4$(IN)$_{12}$(H_2-O)$_6$]·Cl_6·4DMF·18H_2O}$_n$ with [$Zr_{48}Ni_6$] nano-cages was constructed to confine Au nanoparticles (Fig. 7a).[51] The porous framework **1**′ exhibited high surface area and good stability which allowed selectively extracting $AuCl_4^-$ ions from electronic waste. The $AuCl_4^-$ was further reduced into Au nanoparticles and thus formed Au nanoparticles@**1**′ hybrid materials (Au NPs@**1**′-x, x = 1, 2, 3, and 4) with different Au nanoparticle

This journal is © The Royal Society of Chemistry 2024

J. Mater. Chem. A, 2024, **12**, 20578–20605 | **20589**

sizes. By controlling loading amounts, the sizes of Au NPs were tunable. Au NPs@**1**′-3 exhibited a FE_{CO} of 95.2% with a current density of 102.9 mA cm^{-2} at −1.1 V and remained stable for more than 15 h. The excellent stability was attributed to the confinement effect of **1**′, which avoided the agglomeration of Au NPs. Inspired by the CO generator of Au and coupling of Cu–N$_4$ active sites, Au nanoneedles were impregnated into PCN-222 MOF (PCN = porous coordination networks) to construct AuNN@PCN-222(Cu) with the assistance of reducibility of carboxylate ligands (Fig. 7b).[188] AuNN@PCN-222(Cu) with metalloporphyrin Cu centers achieved an FE of 52.5% for C$_2$H$_4$ and exhibited better structural stability. Through *operando* X-ray spectroscopy, *in situ* infrared spectroscopy and DFT calculations, the enhanced selectivity was ascribed to the C–C coupling in a tandem catalysis mechanism. CO was generated at the Au nanoneedles and then abducted to another *CHO at the Au-activated N motifs. The catalyst thus exhibited excellent C$_2$H$_4$ selectivity and high FE. Furthermore, the Au-inserted catalyst also showed improved structural stability, due to the altered charge conduction pathway bypassing the reticular network. A similar case of an electron-conductive polypyrrole (PPy) molecule was also reported, which was inserted into the channel of MOFs through the *in situ* low-temperature polymerization of

pyrrole in the pore of PPy@MOF-545-M (M = Fe, Co, and Ni) (Fig. 7c).[189] MOF-545-Co with increased electron-transfer ability presented excellent electrocatalytic CO$_2$RR performance. The FE_{CO} of PPy@MOF-545-Co reached 98% at −0.8 V, which was approximately two times higher than that of bare MOF-545-Co. Such high performance was attributed to the incorporation of PPy that serves as an electric cable in the channel of MOFs, facilitating electron transfer during the CO$_2$RR process.

5. MOF derivatives

MOFs usually face many challenges, such as limited active sites, unsatisfactory electrical conductivity, and stability issues. This results in the generation and development of MOF derivatives with robust structures and good conductivity as electrocatalysts for the CO$_2$RR.

5.1 MOF derivatives through the wet chemistry method

The structural transformation strategy by the wet chemistry method to obtain MOF derivatives at mild temperature is fascinating as it maximizes the preservation of the original coordination structure and geometric morphology. As an example, S-HKUST-1 was prepared by immersing HKUST-1 in
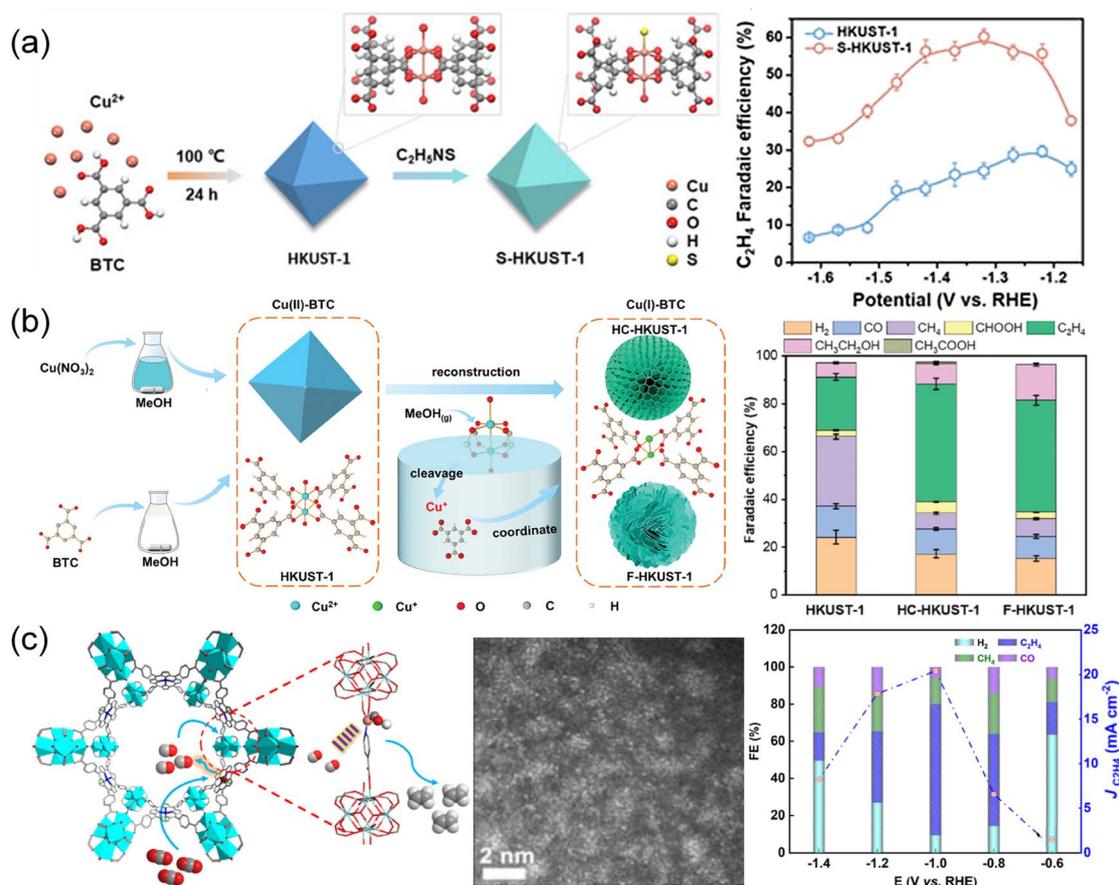

Fig. 8 (a) Schematic illustration depicting the preparation of S-HKUST-1 and FE of C$_2$H$_4$ at different potentials.[132] Copyright 2021, Wiley-VCH. (b) Schematic illustration of the synthetic procedures for HC-HKUST-1 and F-HKUST-1.[190] Copyright 2024, Wiley-VCH. (c) Schematic illustration of the Cu–SAs@Ir–PCN-222-PA tandem electrocatalyst.[53] Copyright 2024, American Chemical Society.

20590 | *J. Mater. Chem. A*, 2024, **12**, 20578–20605

This journal is © The Royal Society of Chemistry 2024

an ethanol solution containing thioacetamide (Fig. 8a).[132] Thioacetamide reacted with the water in HKUST-1 to produce H_2S, facilitating the formation of Cu–S bonds. The element distribution, XRD and Fourier transform infrared spectra indicated that sulfur is distributed throughout the S-HKUST-1 particle, with the framework structure and organic bonding of HKUST-1 well maintained. *Operando* X-ray absorption and systematic characterization confirmed the stable Cu–S motif of S-HKUST-1 during the CO_2 reduction reaction. The atomically dispersed Cu–S units in S-HKUST-1 exhibited high selectivity to C_2H_4 with a maximum FE of 60.0% in an H-type cell and up to 57.2% in a flow cell. The partially oxidized $Cu^{\delta+}$ at the Cu/Cu_xS_y interfaces and the optimized geometric and electronic structures for *CO dimerization, played a crucial role in reducing the kinetic barriers for the CO_2 reduction process. Utilizing a "reduction-cleavage-recrystallization" method (Fig. 8b),[190] Cu(II)-BTC (HKUST-1) underwent a conversion to Cu(I)-BTC facilitated by methanol vapor, followed by reconstruction in a methanol solution. The liquid/solid–gas interface played an important role in the transformation into Cu(I)-BTC, altering the oxidation state of Cu and the coordination environment of the metal node. Cu(I)-BTC showed improved C_2H_4 selectivity with an FE up to 57% at −1.6 V and exceptional durability for over 38 h, superior to both the flower-like HKUST-1 (F-HKUST-1) and HKUST-1 catalysts. The superior performance was attributed to the Cu(I)–O coordinated structure and the presence of free carboxyl groups, which enhanced the dimerization of *CO intermediates and hindered the hydrogenation of *CO intermediates. In another report, Cu single atoms were incorporated into the Ir–PCN-222 MOF to create Cu–SAs@Ir–PCN-222–PA by stirring a mixture of metal precursor Cu–PA (PA = 4-picolinic acid) and Ir–PCN-222–PA at 140 °C for 12 h (Fig. 8c).[53] The dual active sites of Ir-porphyrin and Cu–SAs enabled tandem catalysis for conversion of CO_2 to C_2H_4. CO was initially produced on Ir-porphyrin and then transferred to the nearby adsorbed *CO intermediate on Cu–SAs to facilitate the C–C coupling process. The tandem catalysis led to the production of C_2H_4 from CO_2 with an FE of 70.9% in a flow cell and 66.9% in an H-cell.

5.2 MOF-derivatives through pyrolysis treatment

The process of structural transformation occurring at elevated temperatures is commonly referred to as pyrolysis or annealing. This process involves not only the reduction of ions to atoms but also the conversion of organic frameworks into carbon skeletons. High-temperature pyrolysis plays a crucial role in the creation of single-atom catalysts (SACs) and the introduction of heteroatoms through doping. This strategy allows for the regulation of the coordination environment of MOF-derived carbonaceous SACs for enhancement of CO_2RR performance.

5.2.1 Metal centers. The metal centers in MOF-derived M–N–C catalysts, akin to pristine MOFs, usually determine the performance of the CO_2RR. A highly ordered hierarchical porous catalyst, HP-FeNC, with Fe–N_4 moieties was prepared through the template method,[193] leading to a maximum FE_{CO} of 96% at −0.5 V and partial current density of −19 mA cm^{-2}. Compared with Fe–N–C catalysts, Ni–N–C catalysts were seldom

reported for CO_2 reduction due to the susceptible breakage of Ni–N bonds at high temperature.[194] However, the deprotonated form of Ni–N–C is dominant in neutral or weakly acidic electrolyte, suppressing HER activity with high-efficiency CO_2RR. With the assistance of $ZnCl_2$ and KCl,[45] a microwave-assisted rapid pyrolysis method was employed to derive the Ni–N–C electrocatalyst from Ni-doped ZIF-8 in just 3 min under an air atmosphere. The obtained Ni_1–N–C-50 with a mass ratio of KCl/Ni-ZIF-8 at 0.50 showcased a Ni–N_4–C configuration and presented a remarkable FE_{CO} of 96% in a flow cell, surpassing the traditional pyrolysis of Ni_1–N–C in a furnace. Mechanistic investigations revealed that the microwave-assisted method assisted by $ZnCl_2$/KCl resulted in abundant defective sites and a mesoporous structure, which facilitated CO_2 activation and accelerated mass transfer. Furthermore, Cu was explored as an intriguing element. In contrast to Fe and Ni, Yuan *et al.*[191] reported a CuO/Cu–NSO_4/CN catalyst produced by incomplete pyrolysis of sulfate-modified CuOS-NBDC MOF at 400 °C in air (Fig. 9a). The anionic groups not only stabilized the metal sites but also modified the electronic structure, which reduced CO_2 to formates with a high FE of 87.4% at −0.5 V. The sulfate played a crucial role in promoting the conversion of CO_2 to carboxyl intermediates, subsequently being hydrogenated to HCOOH. The universal modification strategy can also be applied to the preparation of Fe-, Co and Ni- and Zn(II)-based catalysts for catalytic reactions.

In addition to the active sites, recognized as independent units, the adjacent metal sites can largely affect the performance of the CO_2 reduction reaction. Jiao *et al.*[46] prepared Fe and Ni single-atom pairs on MOF-derived N-doped carbons (Fe_1–Ni_1–N–C) by the direct pyrolysis of MOFs. Due to the synergistic effect of Fe and Ni atom pairs, the Fe_1–Ni_1–N–C catalyst presented better selectivity for electrocatalytic reduction of CO_2 to CO than Fe_1–N–C and Ni_1–N–C catalysts. Theoretical simulations revealed that single Fe atoms can be highly activated by adjacent Ni *via* non-bonding interactions in Fe_1–Ni_1–N–C, significantly facilitating the formation of COOH* intermediates and thereby accelerating the overall CO_2 reduction. Similarly, a series of atomically dispersed and nitrogen coordinated dual-metal sites (ZIF–NC–Ni–Fe, ZIF–NC–Fe–Co, and ZIF–NC–Ni–Co) were designed (Fig. 9b).[86] Among these, the ZIF–NC–Ni–Fe catalyst exhibited the most efficient CO_2RR activity, achieving a maximum FE_{CO} of 97.8% at −0.6 V, surpassing ZIF–NC–Fe–Co (FE_{CO} = 76.3%) and ZIF–NC–Ni–Co (FE_{CO} = 68.9%). After characterization and theoretical prediction, it was confirmed that the most active N-coordinated dual-metal site was 2N-bridged (Fe–Ni)N_6, where FeN_4 and NiN_4 moieties were shared with two N atoms. The redistributed electrons on the Fe and Ni atoms in ZIF–NC–Ni–Fe led to an optimal synergistic effect between the two metals, which facilitated *COOH adsorption and *CO desorption kinetics while suppressing the HER. In another report, a CuNi atomic cluster embedded Ni/Cu dual atomic site catalyst (CuNiAC@Ni/Cu–N–C) was designed (Fig. 9c).[192] The introduction of Cu_3Ni atomic clusters into N_4Ni/CuN_3 dual sites enhanced the electronic conductivity and decreased the energy barrier. Therefore, CuNiAC@Ni/Cu–N–C showed excellent performance with
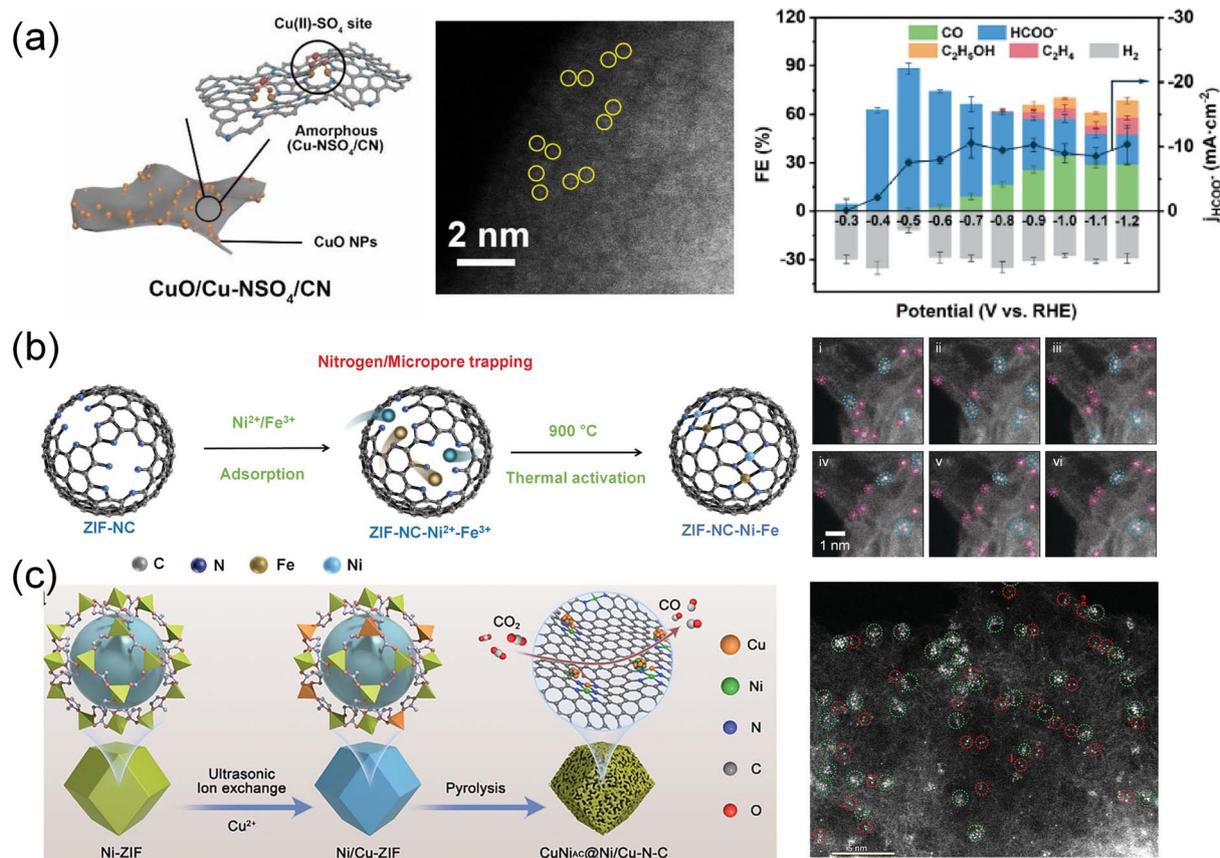
This journal is © The Royal Society of Chemistry 2024

J. Mater. Chem. A, 2024, **12**, 20578–20605 | **20591**

Fig. 9 (a) Schematic illustration of the structure, aberration-corrected HAADF-STEM and FE of CuO/Cu−NSO$_4$/CN.[191] Copyright 2024, Wiley-VCH. (b) Schematic illustration and HAADF-STEM of dual metal Ni−Fe sites in ZIF−NC−Ni−Fe.[86] Copyright 2022, Wiley-VCH. (c) Schematic diagram depicting the preparation of CuNiAC@Ni/Cu−N−C.[192] Copyright 2024, Wiley-VCH.

a maximum FE$_{CO}$ of 98.2% at −0.7 V and maintained continuous electrocatalysis for 70 h.

5.2.2 Nitrogen coordination environment engineering. The preceding section highlighted the significant role of metal centers, typically M−N$_4$, following structural transformation at high temperature. Apart from the ion reduction during the pyrolysis process, the coordination environment also fluctuates under various conditions, including temperature and atmosphere. Through a thermal treatment method involving dicyandiamide,[76] the fabrication of structural Fe−N$_5$ units on defective porous carbon nanofibers (Fe−N$_5$/DPCF) was performed. Fe−N$_5$/DPCF exhibited a maximal FE$_{CO}$ of 93.1%, ascribed to the enhanced electronic localization that facilitated CO desorption and reduced the energy barrier for the CO$_2$RR. Jin *et al.* also accomplished asymmetric coordination of Fe single-atom catalysts (Fig. 10a),[47] forming an Fe−S$_1$N$_3$ unit with three N atoms and one S atom. Compared with Fe−N$_4$ (91.53%) and Fe−B$_1$N$_3$ (90.17%), the catalyst with Fe−S$_1$N$_3$ active sites showed a maximum FE$_{CO}$ of 99.02% at −0.5 V and a TOF of 7804.34 h^{-1}. *Operando* XAFS results combined with DFT calculations revealed that the larger geometric radius of S atoms resulted in geometric distortion in the Fe−S$_1$N$_3$ sites, triggering self-relaxation behavior during intermediate adsorption. Analogous instances, such as the Ga atom in a Ga−N$_3$S-PC configuration, have also been reported.[73]

By manipulating pyrolysis temperatures, low-coordinated Ni−N$_x$ sites were synthesized by replacing the atomically dispersed Zn sites with Ni atoms in a post-synthetic metal substitution strategy (Fig. 10b).[48] The prepared Ni−N$_3$−C catalyst showed excellent CO selectivity with an FE$_{CO}$ of 95.6% and a TOF of 1425 h^{-1} at −0.65 V, superior to the Ni−N$_4$−C catalyst. DFT calculations revealed that low-coordinated Ni−N$_3$−C active sites significantly enhanced COOH* formation, thereby promoting CO$_2$ conversion. By varying pyrolysis temperatures, significantly fewer low-coordinated Ni−N$_2$−C sites were synthesized through a host-guest cooperative protection strategy involving the introduction of polypyrrole into a bimetallic MOF (MgNi−MOF-74).[34] The resulting catalyst, NiSA−N$_2$−C, displayed high FE$_{CO}$ (98%) and TOF (1622 h^{-1}), surpassing the performance of NiSA−N$_3$−C and NiSA−N$_4$−C. The coordination environment, which encompasses not only the amounts but also the types of N atoms, played a crucial role in these disparities. Through the pyrolysis of Ni ZIF-8 within the temperature range of 800 °C to 1000 °C (Fig. 10c), the ratio of pyrrolic N/pyridinic N increased from 0.37 to 1.01 as well as Ni−N$_x$ sites with a decreased coordination number from 3.14 to 2.63.[89] The pyrrolic N-stabilized Ni SAC-1000 showed heightened activity with an FE$_{CO}$ of 98.24% at −0.8 V, surpassing Ni SAC-800 with an FE$_{CO}$ of 40.76% at −0.8 V. DFT calculations revealed that the synergistic effect of the pyrrolic N and low-coordinated Ni could
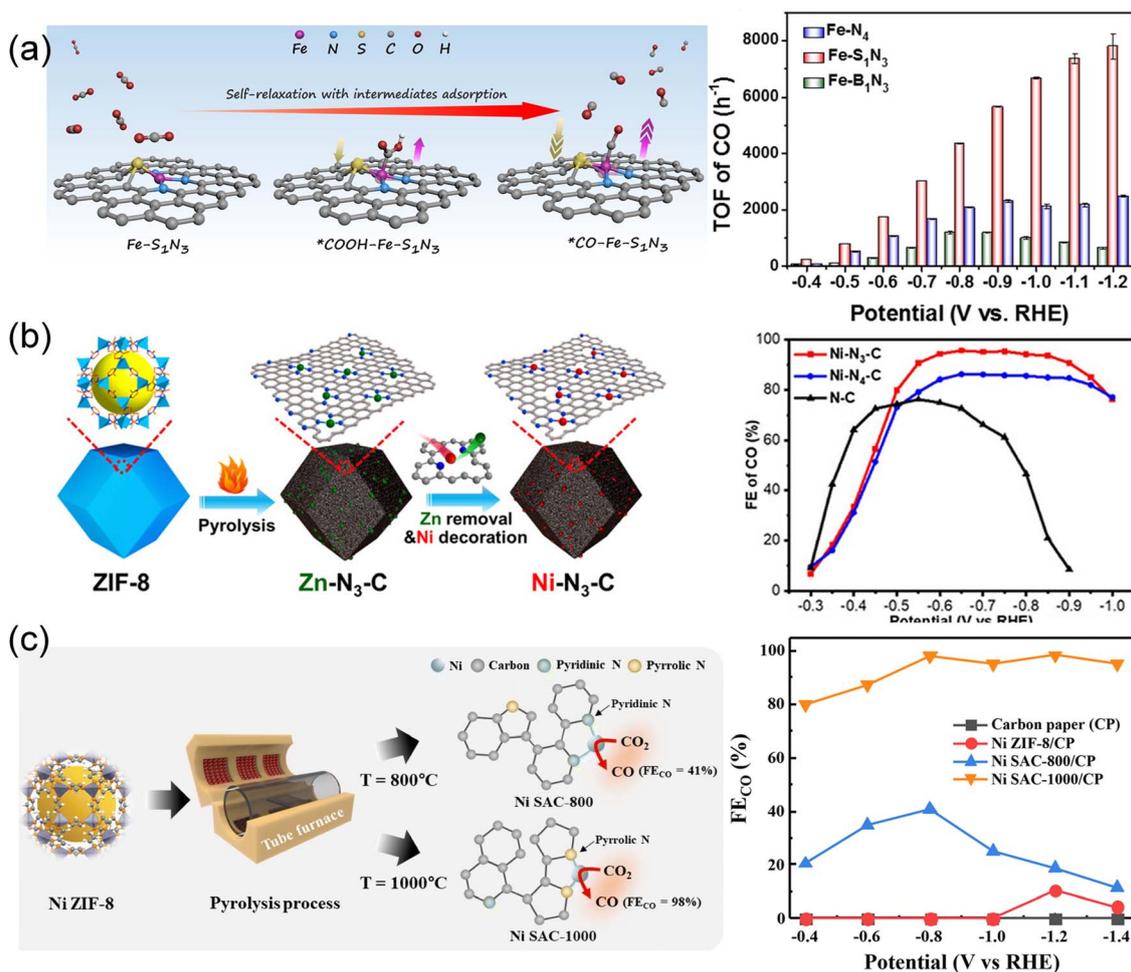
20592 | *J. Mater. Chem. A*, 2024, **12**, 20578–20605

This journal is © The Royal Society of Chemistry 2024

Fig. 10 (a) Schematic illustration showcasing the structural distortion of the Fe−S₁N₃ site with various adsorbed intermediates.[47] Copyright 2023, Wiley-VCH. (b) Schematic illustration for the fabrication of low-coordination single-atom Ni electrocatalysts.[48] Copyright 2021, Wiley-VCH. (c) Schematic illustration for the fabrication of pyrrolic N-stabilized low-coordinated Ni SAC and FE_{CO} at different potentials.[89] Copyright 2024, Royal Society of Chemistry.

decreased the desorption energy barrier of *CO during the CO_2RR, promoting the conversion of CO_2 to CO.

5.2.3 Other heteroatom coordination environment engineering. In addition to N atoms, the coordination of single-atom catalysts with other heteroatoms also significantly influences the electrocatalytic performance, recognized as a significant contributor to tuning of MOF-derived electrocatalysts. In fact, the coordination environment of other heteroatoms (such as O, P, S, Cl, *etc.*) including quantity and types has also been reported to significantly influence the electrocatalytic performance of the CO_2RR.[195]

Recent literature has brought attention to the often-overlooked O atoms. Zhang *et al.*[54] reported an O-coordinated FeN_4 active site (FeN_4–O) through the pyrolysis of an O- and N-rich MOF (Fe-IRMOF-3) as shown in Fig. 11a. The atomically dispersed FeN_4–O active sites broke the symmetrical structure of Fe–N_4 sites and exhibited a superior catalytic performance compared to FeN_4, reaching an FE_{CO} of 95% at −0.50 V and showing excellent stability over 30 h. The enhanced performance was attributed to the axial O coordination, which not

only regulated the binding energy of intermediates and shifted the d-band center of Fe-3d orbitals, facilitating CO desorption, but also inhibited competitive hydrogen production. A similar modulation of the asymmetric atomic interface was also observed in Cu single-atom catalysts prepared by pyrolyzing Cu–Zn/MOF-74.[83] The catalyst with CuN_3O/C active sites delivered a higher FE_{CO} of 96% at −0.8 V compared to $CuCO_3/C$ (FE_{CO} of 20.0% at −0.5 V) and a higher TOF up to 2782.6 h⁻¹. DFT calculations revealed that the incorporation of N and O atoms in CuN_3O/C helped regulate the asymmetric atomic interface, leading to reduction in the Gibbs free energy of CO* desorption and ultimately improving catalytic performance.

S atoms, possessing lower electronegativity to N atoms, can also alter the electronic structure through the formation of M–S bonds. Yang *et al.*[80] synthesized a S/N co-coordinated Ni single-atom catalyst (Ni-SNC) by pyrolysis of a SO_4^{2-} doped Zn/Ni ZIF. The Ni atom interacted with 3 N atoms and a S atom to form an unsaturated Ni–N_3–S active site. The unsaturated Ni–N_3–S active site reduced the energy barrier of $CO_2 \rightarrow COOH*$ conversion in the CO_2RR process and S further improved the current density.

This journal is © The Royal Society of Chemistry 2024

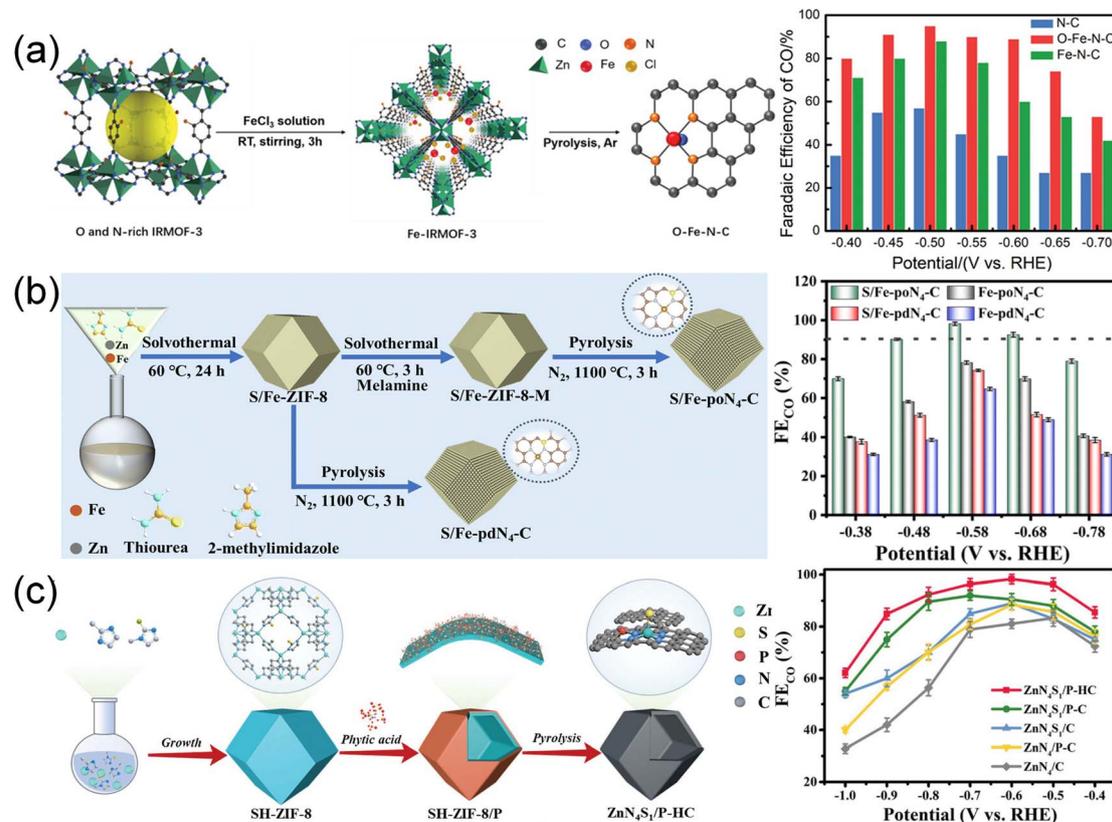*J. Mater. Chem. A*, 2024, **12**, 20578–20605 | **20593**

Fig. 11 (a) Schematic synthesis of O−Fe−N−C and FE$_{CO}$ in CO$_2$-saturated 0.5 M KHCO$_3$. Copyright 2022, Wiley-VCH.[54] (b) Schematic illustration of preparing S/Fe-poN$_4$-C. Copyright 2024, Royal Society of Chemistry.[88] (c) Schematic illustration of the synthesis of ZnN$_4$S$_1$/P-HC. Copyright 2023, Wiley-VCH.[96]

A similar approach involved the incorporation of S and N atoms into the atomically dispersed pyrrole-type Fe–N$_4$ through a series of "solvothermal–solvothermal–pyrolysis" treatments, featuring p–d orbital hybridization in the second coordination layer (Fig. 11b).[88] The S-doped pyrrole-type Fe–N$_4$ electrocatalyst (S/Fe-poN$_4$-C) not only modulated the electron density of the Fe site, facilitating the desorption of *CO, but also compressed H$_2$ evolution. This catalyst exhibited outstanding performance, achieving an FE$_{CO}$ of 98% and a TOF of 4621.2 h^{-1}. *In situ* characterization and calculations indicated that the p–d orbital hybridization balanced the adsorption of *COOH and *CO and accelerated the proton transfer.

P atoms also exhibit a lower electronegativity compared to N atoms, often enhancing the catalytic activity through alterations in the coordination environment and optimization of the adsorption process.[196,197] Reports have highlighted similar catalytic sites of Ni–P$_1$N$_3$ and Fe–P nanocrystals anchored in N-doped carbon polyhedra.[197,198] Recently, Hu *et al.*[95] constructed a three-dimensional ordered microporous structure with ZnN$_4$ sites embedded in P-functionalized carbon (H-3DOM-ZnN$_4$/P–C). The rich hollow walls exposed more active sites while P atoms could adjust the electronic structure of ZnN$_4$ sites, optimizing the adsorption of *COOH intermediates. H-3DOM-ZnN$_4$/P–C showed approximately 100% FE$_{CO}$ at −0.6 V and a high TOF up to 7.8×10^4 h^{-1} at −1.0 V. Subsequently, they

reported a S and P co-doped CO$_2$RR electrocatalyst, denoted as ZnN$_4$S$_1$/P-HC, employing a "synergistically near- and long-range regulation" strategy (Fig. 11c).[96] Zn–N$_4$ was decorated with an axial S ligand in the first coordination and adjacent P atom in the second coordination, leading to an enhancement of charge density in Zn sites. The optimization improved the adsorption of *COOH intermediates, resulting in exceptional performance with FE$_{CO}$ close to 100% at −0.6 V.

6. Stability and reconstruction issues

The CO$_2$RR is usually performed at various reduction potentials, which may lead to the reduction of metal ions of MOFs under certain circumstances. For example, bismuth (Bi) based electrocatalysts are considered environmentally friendly for producing formates due to low toxicity and inert HER activity.[199–201] Lamagni *et al.*[52] reported that Bi(1,3,5-tris(4-carboxyphenyl)benzene) MOF, denoted as Bi(btb), underwent an *in situ* structural rearrangement under CO$_2$RR conditions, forming well-dispersed and highly active Bi nanoparticles for CO$_2$ conversion (Fig. 12a). Interestingly, the inherent poor conductivity of Bi(btb) was overcome by the structural rearrangement. Following CO$_2$RR testing, FE of formates reached 95% at an overpotential of 770 mV, with a mass activity of up to 261(13) A g^{-1} achieved. Cao *et al.*[111] prepared atomically thin

20594 | *J. Mater. Chem. A*, 2024, **12**, 20578–20605

This journal is © The Royal Society of Chemistry 2024

bismuthene (Bi-ene) by *in situ* electrochemical transformation of bismuth-based metal–organic layers (Fig. 12b). The as-obtained Bi-ene exhibited a high selectivity (∼100% FE) for formates, good stability in a broad potential range exceeding 0.35 V and ultrahigh current densities over 300 mA cm^{-2}. Attenuated Total Reflection Fourier-Transform Infrared (ATR-FTIR) spectroscopy and DFT calculations indicated that formate was produced *via* the OCHO* intermediate, and the adsorbed HCO_3^- was found to have key roles in the CO_2RR. Yao *et al.*[104] investigated a Bi-MOF constructed from bismuth oxy-iodide and H_3BTC (benzene-1,3,5-tricarboxylic acid), demonstrating that electrolyte and potential mediated the restructuring processes (Fig. 12c). The Bi-MOF transformation into $Bi_2O_2CO_3$ and subsequent reduction to Bi played a pivotal role in determining morphology, defects, composition, and valence states, leading to enhanced formate yields and partial current densities. The resulting Bi nanosheets showed a maximum FE_{HCOO^-} of 92% at −1.1 V and a partial current density of −15 mA cm^{-2} at −1.3 V. The presence of unsaturated Bi atoms facilitated *OCHO intermediate adsorption, contributing to improved reaction efficiency. Huang *et al.*[202] further studied the transformation process of Bi-BTC (formed using Bi irons and H_3BTC) and its CO_2RR performance. The transformation of the column Bi-BTC structure into nanosheets was influenced by the breaking of the Bi–O bond. And the exposed

(020) crystal plane of restructured $Bi_2O_2CO_3$ favored *OCHO intermediate interactions. As a result, it achieved an FE of 96% and a current density of 25 mA cm^{-2}. These studies underscored the significance of surface restructuring *via* electrochemical methods for developing high-performance and durable electrocatalysts.

Recently, the reconstruction of Cu-based MOFs was also investigated. Cu with low valence usually exhibits enhanced reactivity for C_2 products. Initially, utilizing an electrochemical conversion method (Fig. 13a), CoS_2 was obtained from a Co-ZIF-L precursor.[203] Subsequently, the CoS_2 template was converted into Cu_2S nanocrystals through an electrochemical cation exchange process. The resulting Cu_2S maintained its original three-dimensional morphology and a high density of grain boundaries. When applied in the CO_2RR process, the catalyst demonstrated notable efficiency in converting CO_2 to formates, achieving an impressive FE of 87.3%. Zhang *et al.*[204] reported coordinatively unsaturated Cu paddle wheel (CU-CPW) clusters in defect-containing HKUST-1 (Cu(II)-BTC) prepared by an atomized trimesic acid and $Cu(OH)_2$ strategy (Fig. 13b). $Cu_2(HCOO)_3$ in CU-CPW is proven to be maintained after the electrochemical structural transformation and serve as the active site. CU-CPW accelerated the PCET process compared with coordinatively saturated $Cu_2(HCOO)_4$, producing hydrocarbons from CO_2. A highly active and selective C_2H_4 electrocatalyst
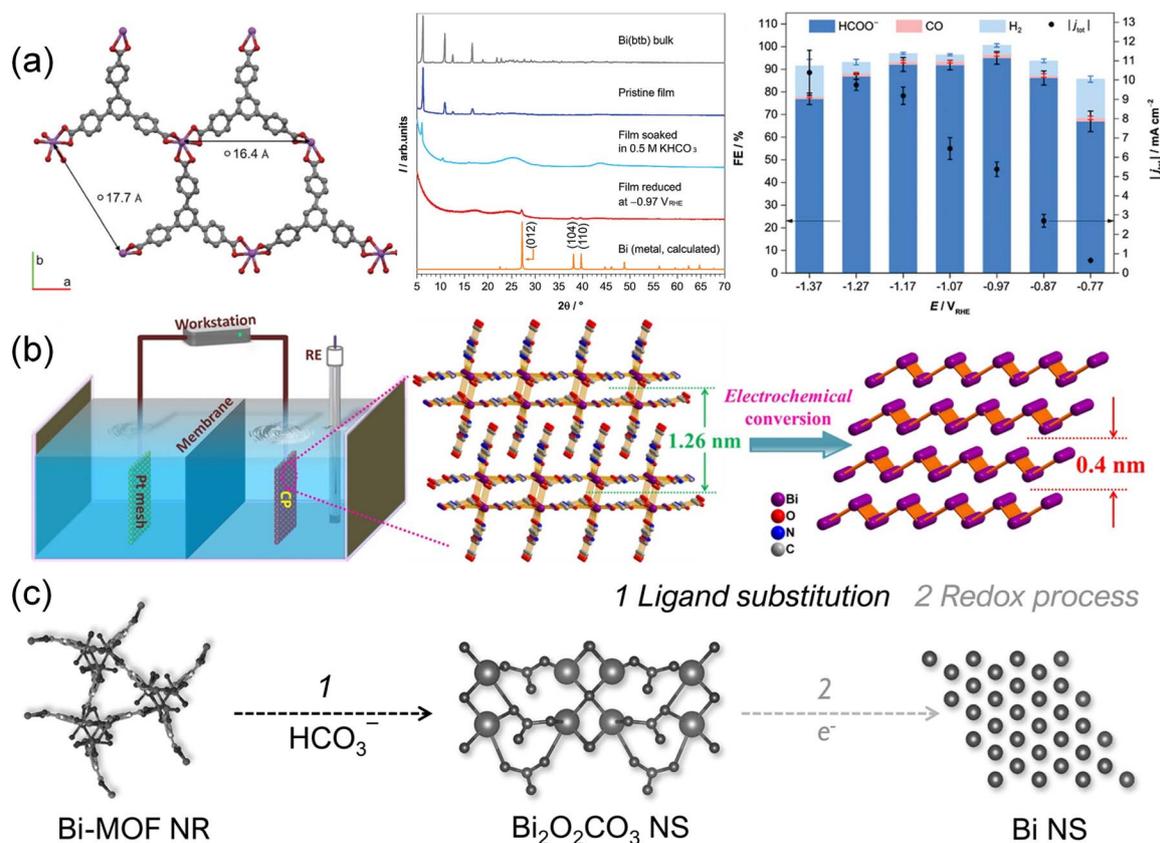

Fig. 12 (a) Structural representation, XRD spectra and FE data of Bi(btb).[52] Copyright 2020, Wiley-VCH. (b) Schematic illustration depicting the preparation of Bi-ene.[111] Copyright 2020, Wiley-VCH. (c) Schematic illustration depicting the *in situ* reconstruction process of Bi-MOF NRs to Bi NSs.[104] Copyright 2021, Wiley-VCH.

This journal is © The Royal Society of Chemistry 2024

J. Mater. Chem. A, 2024, **12**, 20578–20605 | **20595**

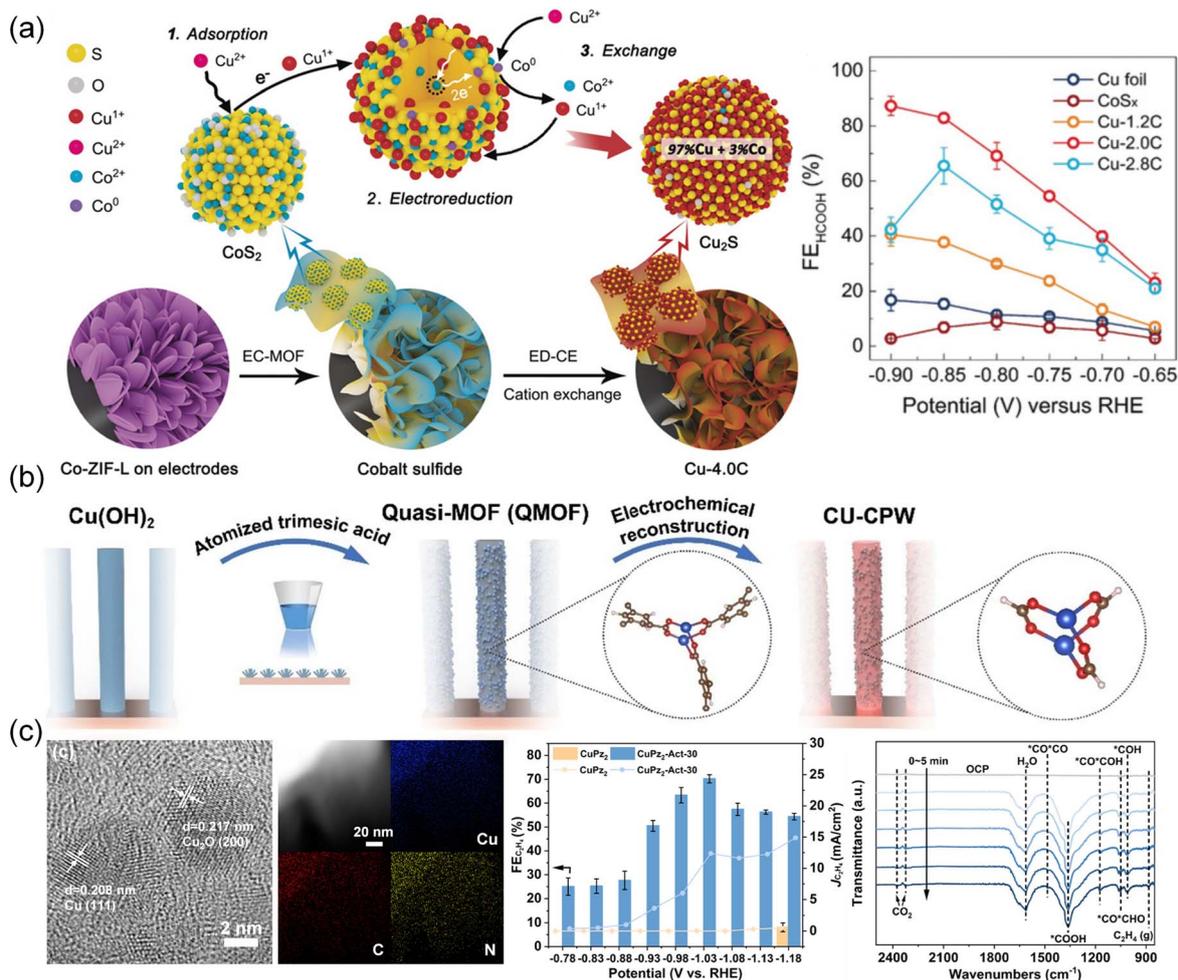Fig. 13 (a) Schematic illustration depicting the pathways/mechanisms for electrochemically driven cation exchange and FE of different catalysts.[203] Copyright 2020, Wiley-VCH. (b) Schematic illustration of the synthetic procedures for CU-CPW.[204] Copyright 2021, Wiley-VCH. (c) HRTEM images of $CuPz_2$-Act-30 with the corresponding elemental mapping, FE of C_2H_4, and in situ ATR-FTIR spectra of $CuPz_2$-Act-30.[134] Copyright 2022, American Chemical Society.

($CuPz_2$-Act-30) derived from MOF $CuPz_2$ (Pz = Pyrazole) with dispersive Cu/Cu_2O nanoclusters was prepared by in situ electrochemical reduction (Fig. 13c).[134] It achieved a high FE of 70.2 ± 1.7% at −1.03 V toward C_2H_4 generation. In situ ATR-FTIR spectroscopy and DFT calculations indicated that the nanoclusters transformed by in situ reconstruction had a preference to adsorb local CO and promote C–C coupling and hydrogenation to produce C_2H_4. Moreover, restructuring multi-phase interfaces of $Ag/Cu/Cu_2OAg_{0.1}$/HKUST-1 in $Ag_{0.1}$/HKUST-1 was achieved by 1 h of electroreduction.[131] By leveraging the higher standard redox potential of Ag and its less negative formation enthalpy of oxides, Ag was expected to stabilize neighboring Cu(I). Tandem electrolysis was enabled by the weak bonding of Ag *CO to Cu(0)–Cu(I) sites. The derived electrocatalysts showed a high FE of 57.2% at −1.3 V for CO_2 conversion to C_2H_4. Characterization and calculations further highlighted the crucial role of Ag in stabilizing Cu(I) and increasing CO surface coverage, while the Cu/Cu_2O interface reduced the energy barrier of C–C coupling. Tandem electrolysis and

electrochemical reduction were also successfully carried out on a [Cu^I(im)] (1) MOF (Im = imidazole),[124] resulting in the synthesis of CuN_2 and Cu_2N_4. The $CuN_2/Cu(111)$ derivatives with Cu–N coordination exhibited superior performance compared to $Cu_2N_4/Cu(111)$ with Cu–N and Cu–Cu coordination. The C_{2+} products including C_2H_4, C_2H_5OH and n-C_3H_7OH were detected and the total $FE_{C_{2+}}$ of CuN_2 reached 64.8%, surpassing the 43.9% efficiency of Cu_2N_4. This study emphasized the crucial role of pristine MOFs as catalysts for facilitating the conversion of CO_2 to CO.

7. Advanced characterization techniques

Though the well-defined structure of MOFs can be tailored to help understand the structure–activity relationship, the electrochemical stability of MOFs would be a major concern for their application. Under the reduction conditions of the CO_2RR, it is common for electrocatalysts undergoing reconstruction to
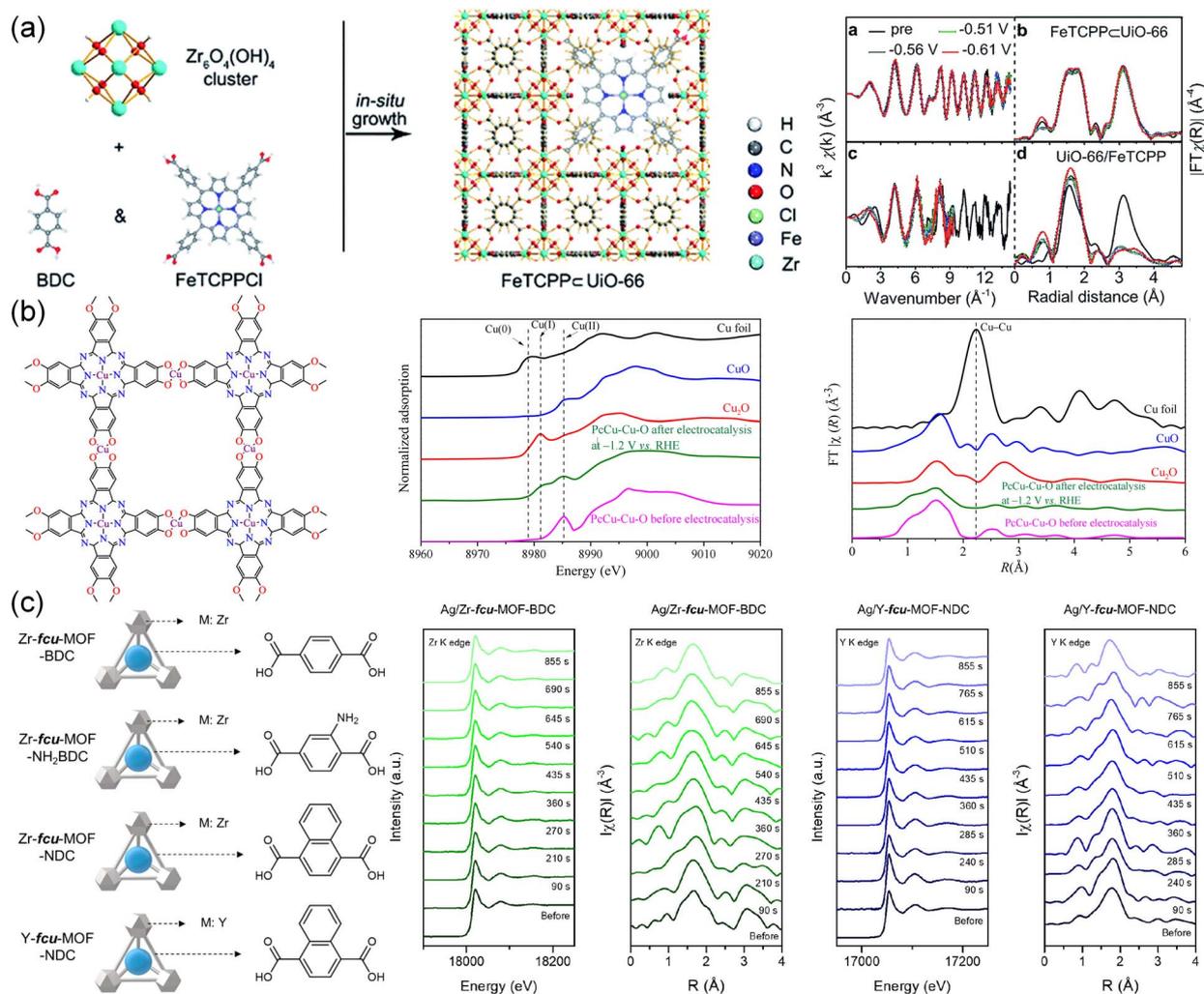
20596 | J. Mater. Chem. A, 2024, 12, 20578–20605

This journal is © The Royal Society of Chemistry 2024

Fig. 14 (a) Schematic of FeTCPP⊂UiO-66 MOF and the Zr K-edge *in situ* EXAFS for FeTCPP⊂UiO-66 and UiO-66/FeTCPP.[94] Copyright 2019, Royal Society of Chemistry. (b) Illustration of the structure, normalized Cu K-edge XANES and Fourier transform EXAFS of PcCu-Cu-O MOF.[127] Copyright 2021, American Chemical Society. (c) Schematic of Zr-*fcu*-MOF-BDC, Zr-*fcu*-MOF-NH₂BDC, Zr-*fcu*-MOF-NDC and Y-*fcu*-MOF-NDC. *Operando* XAS analysis of the Zr K-edge XANES and EXAFS of Ag/Zr-*fcu*-MOF-BDC and the Y K-edge XANES and EXAFS of Ag/Y-*fcu*-MOF-NDC.[77] Copyright 2020, American Chemical Society.

build new active sites.[104,134,205,206] For example, Cu centers in Cu₃(HITP)₂ would be irretrievably reduced to Cu⁰ at negative potential.[133] Cu clusters were detected during the CO₂RR from Cu dimers in HKUST-1, and Cu/CuₓSᵧ interfaces were reconstructed from S-HKUST-1 (with a Cu–S motif on HKUST-1) under CO₂RR conditions.[104,126,132] Therefore, it is important to monitor the structural changes of electrocatalysts during reactions to probe into the origin of the CO₂RR on MOFs using *in situ* techniques. In addition, dynamic electrode/electrolyte interfaces can also be monitored to shed light on the reaction mechanisms.

7.1 *In situ* XAS for probing active sites at the atomic level

XAS has emerged as a popular technique to detect the local structure around single metal atoms, which is not limited to the state of samples under testing. It can provide valuable information on the oxidation state, the local coordination

environment, and the electronic structure of the material.[207] The changes in metal nodes and the coordination environment surrounding metal active centers can be reflected in the *in situ* XAS spectra to monitor the CO₂RR dynamics at the atomic level.[208]

As shown in Fig. 14a, (5,10,15,20-tetrakis(4-carboxyphenyl)porphyrinato)-Fe(III) chloride (FeTCPPCl) was introduced into UiO-66 to form a robust active MOF (FeTCPP⊂UiO-66) with two carboxylic ligands.[94] FeTCPP⊂UiO-66 realized nearly 100% selectivity for converting CO₂ to CO. *In situ* near edge XAS displayed almost unchanged curves at different potentials compared to the initial state, which demonstrated the structural stability of FeTCPP⊂UiO-66 in an electrochemical environment. However, the wavenumber of the oscillation curve for UiO-66/FeTCPP (the physical mixture of FeTCPP and UiO-66) descended distinctly at −0.51 V, indicating its structural collapse. Due to the robust structure and protonation facilitator
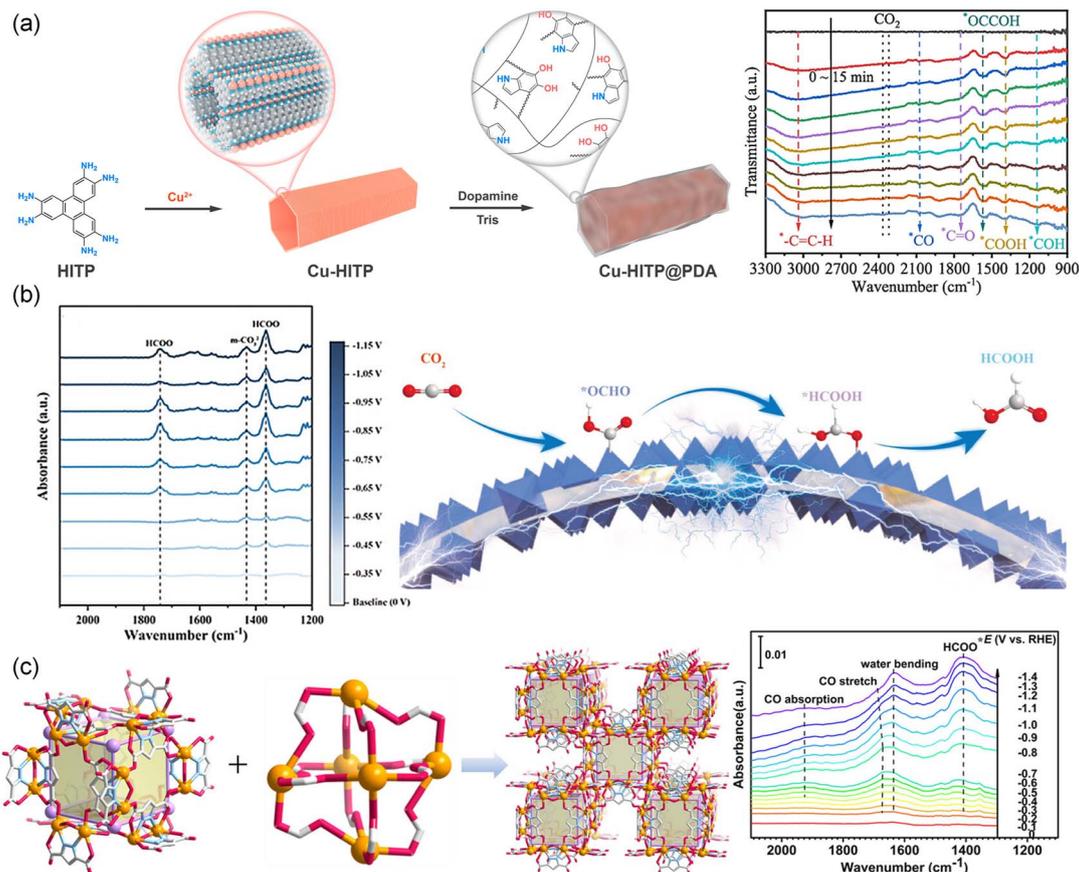
This journal is © The Royal Society of Chemistry 2024

J. Mater. Chem. A, 2024, 12, 20578–20605 | 20597

Fig. 15 (a) Schematic of Cu-HITP@PDA and *in situ* FTIR spectra on Cu-HITP.[129] Copyright 2022, American Chemical Society. (b) *In situ* FTIR spectra of Cu@Bi$_{1/2}$ at various potentials and the schematic diagram of the CO$_2$RR.[209] Copyright 2023, Wiley-VCH. (c) Schematic of PZH-1 and *in situ* FTIR spectra of PZH-1.[102] Copyright 2023, Wiley-VCH.

of FeTCPP⊂UiO-66, the PCET pathway on the iron porphyrin sites was facilitated, leading to a low overpotential. Similarly, no significant changes in the *in situ* XAS spectra of the PcCu-Cu-O MOF catalyst confirmed its stability during the CO$_2$RR as shown in Fig. 14b.[127] The stability of Ag/Zr-*fcu*-MOF-BDC with Ag-incorporated was also investigated by *operando* XAS (Fig. 14c).[77] The oxidation states, coordination number and atomic distance showed no observable difference during and after the reaction as shown in the Zr K-edge X-ray absorption near edge structure (XANES) and extended X-ray absorption fine structure (EXAFS) spectra, indicating a constant Zr oxidation state and robust structure of Ag/Zr-*fcu*-MOF-BDC. This was also found in the Y K-edge XANES and EXAFS spectra of Ag/Y-*fcu*-MOF-NDC, suggesting that the Zr- and Y-based MOFs with varying organic linkers and the metal nodes remained stable during the CO$_2$RR.

7.2 *In situ* FTIR and Raman spectroscopy for monitoring dynamic interfaces

FTIR (Fourier-transform infrared spectroscopy) and Raman spectroscopy are useful spectroscopic techniques for capturing reaction intermediates on the surface of catalysts and providing information related to reaction products and pathways. By

using FTIR and Raman spectroscopy, the vibration modes of chemical bonds and structural coordination of the intermediates during the CO$_2$RR can be acquired. However, FTIR is usually interfered with by the water absorption peak in aqueous solution, which makes it a great challenge to monitor intermediates when applied in aqueous solution. Instead of measuring the absorption of light like FTIR, Raman spectroscopy based on the scattering of light can compensate for this drawback due to weak light scattering by water.[210]

In situ FTIR spectroscopy was reported to capture intermediates on the catalyst surface during the CO$_2$RR. Fig. 15a shows the *in situ* FTIR spectra of Cu-HITP.[129] The bands at 1387 and 1400 cm^{-1} were assigned to the *COOH and *COO, while the band at 2079 cm^{-1} was assigned to the chemisorbed *CO. The absorption bands of the *CH$_2$ intermediate were also observed (3108 cm^{-1} and 995 cm^{-1}). The band at 1150 cm^{-1} was attributed to the *COH, indicating the hydrogenation of *CO into *COH. Additionally, the band at 1575 cm^{-1} indicated the existence of *OCCOH, which meant that *OCCOH was a key intermediate for CO$_2$ conversion to C$_{2+}$ products. Similarly, a MOF-on-MOF (Cu@Bi$_{1/2}$, CAU-17 and ZJU-199) copper-based catalytic electrode was prepared by *in situ* synthesis on a foamed copper substrate[209] and studied using *in situ* FTIR to reveal the mechanism of HCOOH formation. As shown in Fig. 15b, the
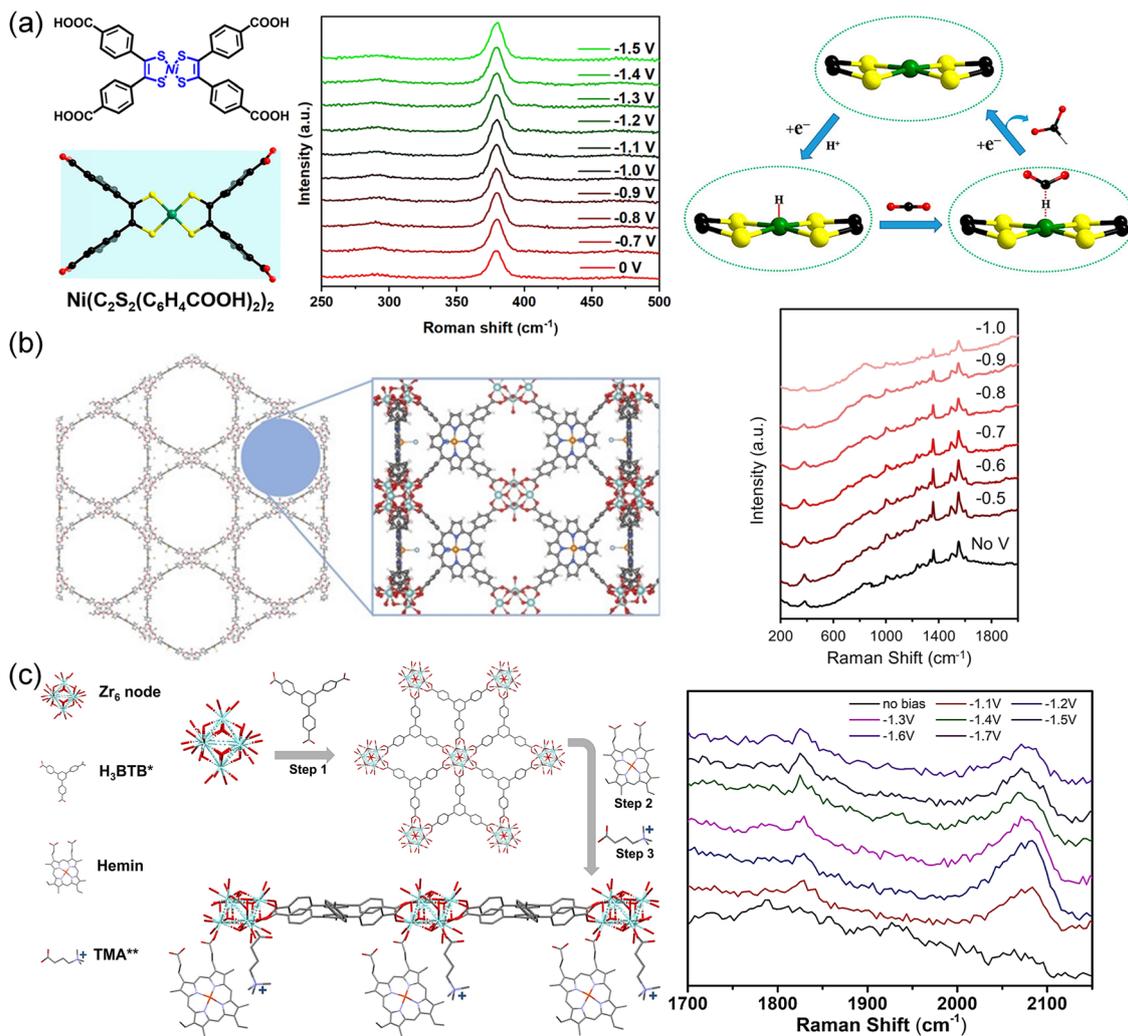
20598 | *J. Mater. Chem. A*, 2024, **12**, 20578–20605

This journal is © The Royal Society of Chemistry 2024

Fig. 16 (a) Ligand structures of [Ni(C$_2$S$_2$(C$_6$H$_4$COOH)$_2$)$_2$], *in situ* Raman spectra of the Ni–S bond in **1″** during the CO$_2$RR process and proposed reaction paths for the formation of HCOO$^-$ on the [NiS$_4$] sites.[99] Copyright 2021, American Chemical Society. (b) Immobilized metalloporphyrin in MOF and *in situ* Raman spectra for each potential for PCN-222(Fe).[211] Copyright 2022, Wiley-VCH. (c) Schematic of Zr–BTB@Hemin-TMA, and *in situ* Raman spectra recorded at different potentials for Zr–BTB@Hemin-TMA.[72] Copyright 2022, Wiley-VCH.

characteristic band located at 1363 cm^{-1} corresponded to the HCOO$^-$ which displayed a trend of increasing and then decreasing with the potential from −0.35 to 0.95 V. In addition, there was a HCOO$^-$ band that appeared at 1743 cm^{-1} different from that of Bi@Cu$_{1/2}$, indicating different reaction ways to generate formic acid. The FE was further improved using a bismuth-based metal–organic framework (PZH-1), which was synthesized through a ligand-directing strategy using pyrazole-3,5-dicarboxylic acid (Fig. 15c).[102] The bismuth-based ZMOF showed an ACO topological structure and strong coordination bonding within the Bi-based cages. *In situ* FTIR spectra of Bi-ZMOF showed a characteristic band of two-oxygen bridged *HCOO (1414 cm^{-1}) at −0.4 V, which was intensified as the potential shifted from −0.4 V to −1.4 V. The band in the range of 1675–1685 cm^{-1} associated with the C=O stretching mode became more prominent as the potential decreased. These findings indicated that the surface-bound Bi–*HCOO species

played a crucial role as active intermediates for forming HCOOH.

The use of *in situ* Raman spectroscopy also provided valuable insights into the stability and reaction mechanisms of various electrocatalytic systems. Isomorphic MOFs (Me$_2$NH$_2$$^+$){In^{III}-[Ni(C$_2S_2$(C$_6H_4$COO)$_2$)$_2$]}·3DMF·1.5H$_2$O (**1″**, DMF = *N,N*-dimethylformamide) and (Me$_2$NH$_2$$^+$)[In^{III}-(TTFTB)]·0.7C$_2H_5$-OH·DMF (**2**, TTFTB = tetrathiafulvalene-tetrabenzoate) were used as electrocatalysts for the CO$_2$RR.[99] The [NiS$_4$] site in **1″** was considered to be the catalytic center and CO$_2$ binding site. Therefore, **1″** showed enhanced CO$_2$RR performance (FE$_{HCOO^-}$ = 89.6%) compared with **2** (FE$_{HCOO^-}$ = 54.7%). As shown in Fig. 16a, *in situ* Raman spectra exhibited no visible change in the CO$_2$RR process, indicating the stability of the catalytic sites.

By immobilizing iron–porphyrin complexes into MOFs (Fig. 16b), PCN-222(Fe) exposed more active sites for the CO$_2$RR toward CO production, which showed an increasing current trend as the potential increased from −0.5 to −1.0 V.[211] *In situ*

This journal is © The Royal Society of Chemistry 2024

J. Mater. Chem. A, 2024, **12**, 20578–20605 | **20599**

Raman spectra suggested that the structure was maintained under electrochemical bias. The characteristic bands of PCN-222(Fe) did not attenuate under electrochemical bias, indicating that no structural reconstruction occurred during the CO_2RR.

As shown in Fig. 16c, a cationic functional group (3-carboxypropyl trimethylammonium) was immobilized to Fe-porphyrin (Hemin)-modified Zr-BTB (termed Zr-BTB@Hemin-TMA) to enhance the activity and selectivity ($\sim$100%).[72] *In situ* Raman spectroscopy conducted at different potentials suggested that two bands at 1840 cm^{-1} and 2060 cm^{-1} were attributed to catalyst-bounded CO stretching, indicating the presence of a weakly bounded CO intermediate. The enhanced selectivity resulted from the electrostatic stabilization provided by the tethered functional group, which facilitated the swift release of CO as a product.

8. Challenges and perspectives

8.1 Challenges

Metal–organic frameworks (MOFs), known for their orderly arrangement, extensive surface area, and adaptable structure, have been applied as electrocatalysts together with their derivatives for the CO_2 reduction reaction (CO_2RR). Different metal centers and surrounding atoms yield distinct reduction products. By selecting appropriate metals and meticulously adjusting the coordination environment, desired reduced carbon products can be obtained. However, their application still faces many challenges due to inherent limitations such as poor conductivity, low chemical stability, and limited density of active sites. Some issues need to be considered in designing highly active and selective electrocatalysts, which we list as follows:

(1) The issue of poor conductivity arises from organic ligands in MOFs, hindering electron transfer during the electrocatalytic reduction process. Despite efforts to enhance conductivity through strategies such as morphological and structural regulation of MOFs, creation of unsaturated metal coordination sites, incorporation of functionalized ligands and/or multimetal components in MOFs, and integration into conductive active materials, the conductivity of two-dimensional (2D) MOFs remains inferior to that of 2D graphene. Improving the conductivity of MOFs is still an important research topic for future advancements in this field.

(2) MOFs bonded with a coordination bond are prone to dissolution in the acidic or alkaline solution, underscoring the critical need to enhance the intrinsic stability of MOFs. Therefore, designing robust MOF catalysts adaptable to diverse environments is highly desirable. It may be considered to use that strategies involve creating acid-resistant MOFs with high-valence state metals (hard acids) and carboxylate ligands (hard bases); developing alkali-resistant MOFs with low-valence state metals (soft acids) and azolate ligands (soft bases); improving the connectivity of building units; tightening or stiffening the ligands; and fortifying MOFs by substituting unstable building units with resilient counterparts for improving stability.

(3) The density of active sites within MOFs is crucial for assessing CO_2RR performance. Active sites within MOFs typically encompass metal centers and/or the surrounding ligands as illustrated in the above-mentioned sections, which have certain and thus limited quantities in a certain MOF structure. Therefore, enhancing the density of active sites in pristine MOFs is also effective in improving the CO_2RR performance, which demands the exploration of newly designed MOFs. In addition, we also propose to incorporate functional guest molecules or elements into the pore channels of MOFs for enhancing the catalytic activity of MOFs toward the CO_2RR, which may increase active sites in another way. Similarly, for MOF derivatives, their active densities can be increased through impregnation methods or other approaches with optimized loading followed by high-temperature pyrolysis.

8.2 Perspectives

Aligned with these challenges and issues to be addressed in the application of MOFs and their derivatives for the CO_2RR, perspectives and future directions are proposed in this section. The metal nodes of MOFs or metal centers of MOF derivatives typically dictate the pathway toward various reduction products, while coordinated organic ligands or the surrounding heteroatoms usually influence the selectivity by adjusting the electron density around the metal nodes or metal centers. Regulation of the metal oxidation state and surrounding coordination environment has been demonstrated to effectively affect the electrochemical performance. Despite considerable efforts in applying MOFs and their derivatives for electrocatalytic CO_2 reduction, designing novel structures with high performance still remains challenging and desirable. Furthermore, mechanisms of existing MOFs and their derivatives need to be clearly studied to guide future structure design and performance improvement. In summary, we believe that future directions for designing and developing novel MOF-based catalysts can be focused on the following:

(1) Rationally designing metal centers: the selection of appropriate metal centers is essential for achieving desired products. The CO_2RR can be extended from single-metal MOF-based catalysts to bimetallic, trimetallic or polymetallic MOFs, which often exhibit enhanced performance due to synergistic effects from the neighboring metal centers.

(2) Engineering the coordination environment: the microenvironment surrounding the metal centers significantly impacts product yield and selectivity. Modifying ligands with coordination functional groups or introducing new functional coordinating ligands by direct synthesis or post-modification within MOFs may be used to improve electrocatalytic CO_2RR performance.

(3) Optimization of conductive substrates or inserted nanocomposites: integrating conductive substrates or nanocomposites with MOFs can significantly decrease interfacial resistance, thereby improving the electron transfer process. Consequently, suitable conductive substrates and/or nanocomposites may be developed for the future synthesis of conductive MOF-based catalysts.

(4) Advanced characterization techniques: utilizing advanced characterization techniques provides an opportunity to unravel the intrinsic active sites and capture reaction intermediates, offering insight into the reaction mechanism. It is desired to further develop advanced *in situ* characterization techniques for monitoring the dynamic changes of MOF-based electrocatalysts and electrode/electrolyte interfaces during the CO_2RR, thereby facilitating the design and synthesis of highly active and selective MOF-based electrocatalysts.

(5) Computational calculations: to support mechanistic studies, computational simulations such as DFT calculations and molecular dynamics are also needed from the perspective of thermodynamics and kinetics of the CO_2RR. Machine learning may also be involved as an effective method for screening MOF-based catalysts.[212] The integration of computational tools will effectively pave the way for rational design of MOF-based catalysts in the CO_2RR.

Data availability

All the data supporting this review have been cited from reported publications, which are indicated throughout this review with copyrights obtained.

Author contributions

Xiaoming Liu: investigation, conceptualization, formal analysis, visualization, writing – original draft review and editing. Xuan-He Liu: supervision, funding acquisition, writing – review and editing. Xiangrui Zhang: writing – review. Huan Wang: review. Qinglan Zhao: supervision, funding acquisition, writing – review and editing.

Conflicts of interest

The authors declare no conflicts of interest.

Acknowledgements

References

1 X. Li, S. Wang, L. Li, Y. Sun and Y. Xie, *J. Am. Chem. Soc.*, 2020, **142**, 9567–9581.

2 C. Hu, S. Bai, L. Gao, S. Liang, J. Yang, S.-D. Cheng, S.-B. Mi and J. Qiu, *ACS Catal.*, 2019, **9**, 11579–11588.

3 H. Liu, Y. Zhu, J. Ma, Z. Zhang and W. Hu, *Adv. Funct. Mater.*, 2020, **30**, 1910534.

4 Z. Liu, Z. Deng, G. He, H. Wang, X. Zhang, J. Lin, Y. Qi and X. Liang, *Nat. Rev. Earth Environ.*, 2022, **3**, 141–155.

5 S. Bhattacharjee, M. Rahaman, V. Andrei, M. Miller, S. Rodríguez-Jiménez, E. Lam, C. Pornrungroj and E. Reisner, *Nat., Synth.*, 2023, **2**, 182–192.

6 X. Chen, X. Su, H.-Y. Su, X. Liu, S. Miao, Y. Zhao, K. Sun, Y. Huang and T. Zhang, *ACS Catal.*, 2017, **7**, 4613–4620.

7 A. M. Appel, J. E. Bercaw, A. B. Bocarsly, H. Dobbek, D. L. DuBois, M. Dupuis, J. G. Ferry, E. Fujita, R. Hille and P. J. Kenis, *Chem. Rev.*, 2013, **113**, 6621–6658.

8 J. Shi, Y. Jiang, Z. Jiang, X. Wang, X. Wang, S. Zhang, P. Han and C. Yang, *Chem. Soc. Rev.*, 2015, **44**, 5981–6000.

9 E. Le Saché and T. Reina, *Prog. Energy Combust. Sci.*, 2022, **89**, 100970.

10 D. He, J. Yan, K. Chen, L. Zhang, J. Lu, J. Liu and Y. Luo, *ACS Catal.*, 2023, **13**, 12114–12124.

11 M. Li, Z. Sun and Y. H. Hu, *Chem. Eng. J.*, 2022, **428**, 131222.

12 J. W. Ko, S.-W. Kim, J. Hong, J. Ryu, K. Kang and C. B. Park, *Green Chem.*, 2012, **14**, 2391–2394.

13 E. W. Lees, B. A. Mowbray, F. G. Parlane and C. P. Berlinguette, *Nat. Rev. Mater.*, 2022, **7**, 55–64.

14 W. Xia, Y. Xie, S. Jia, S. Han, R. Qi, T. Chen, X. Xing, T. Yao, D. Zhou and X. Dong, *J. Am. Chem. Soc.*, 2023, **145**, 17253–17264.

15 D. Song, Y. Lian, M. Wang, Y. Su, F. Lyu, Z. Deng and Y. Peng, *eScience*, 2023, **3**, 100097.

16 Z. Ma, T. Wan, D. Zhang, J. A. Yuwono, C. Tsounis, J. Jiang, Y.-H. Chou, X. Lu, P. V. Kumar and Y. H. Ng, *ACS Nano*, 2023, **17**, 2387–2398.

17 S. Yang, M. Jiang, W. Zhang, Y. Hu, J. Liang, Y. Wang, Z. Tie and Z. Jin, *Adv. Funct. Mater.*, 2023, **33**, 2301984.

18 P. Saha, S. Amanullah and A. Dey, *Acc. Chem. Res.*, 2022, **55**, 134–144.

19 S. Banerjee, C. S. Gerke and V. S. Thoi, *Acc. Chem. Res.*, 2022, **55**, 504–515.

20 G. Wen, B. Ren, Y. Zheng, M. Li, C. Silva, S. Song, Z. Zhang, H. Dou, L. Zhao and D. Luo, *Adv. Energy Mater.*, 2022, **12**, 2103289.

21 S. Jin, Z. Hao, K. Zhang, Z. Yan and J. Chen, *Angew. Chem., Int. Ed.*, 2021, **60**, 20627–20648.

22 W. Lai, Y. Qiao, Y. Wang and H. Huang, *Adv. Mater.*, 2023, **35**, 2306288.

23 X. Wang, Y. Jiang, K. Mao, W. Gong, D. Duan, J. Ma, Y. Zhong, J. Li, H. Liu and R. Long, *J. Am. Chem. Soc.*, 2022, **144**, 22759–22766.

24 D. Sun, X. Xu, Y. Qin, S. P. Jiang and Z. Shao, *ChemSusChem*, 2020, **13**, 39–58.

25 Y. Kim, B. Kim, H. Choi, S. Kim, Y. Yun and J. Oh, *Chem. Eng. J.*, 2023, **461**, 142126.

26 Z. Ma, C. Tsounis, C. Y. Toe, P. V. Kumar, B. Subhash, S. Xi, H. Y. Yang, S. Zhou, Z. Lin and K.-H. Wu, *ACS Catal.*, 2022, **12**, 4792–4805.

27 L. Gao, S. Bai, Y. Zhang and C. Hu, *ChemCatChem*, 2022, **14**, e202200383.

28 Y. Yao, W. Zhuang, R. Li, K. Dong, Y. Luo, X. He, S. Sun, S. Al-Faifi, X. Sun and W. Hu, *Chem. Commun.*, 2023, **59**, 9017–9028.

This journal is © The Royal Society of Chemistry 2024

J. Mater. Chem. A, 2024, **12**, 20578–20605 | **20601**

29 M. Zhang, M. Lu, M.-Y. Yang, J.-P. Liao, Y.-F. Liu, H.-J. Yan, J.-N. Chang, T.-Y. Yu, S.-L. Li and Y.-Q. Lan, *eScience*, 2023, **3**, 100116.

30 A. Xu, S.-F. Hung, A. Cao, Z. Wang, N. Karmodak, J. E. Huang, Y. Yan, A. Sedighian Rasouli, A. Ozden and F.-Y. Wu, *Nat. Catal.*, 2022, **5**, 1081–1088.

31 S. Liu, H. Tao, Q. Liu, Z. Xu, Q. Liu and J.-L. Luo, *ACS Catal.*, 2018, **8**, 1469–1475.

32 R. Zhao, Y. Wang, G. Ji, J. Zhong, F. Zhang, M. Chen, S. Tong, P. Wang, Z. Wu and B. Han, *Adv. Mater.*, 2023, **35**, 2205262.

33 T. Tang, Z. Wang and J. Guan, *Adv. Funct. Mater.*, 2022, **32**, 2111504.

34 Y. N. Gong, L. Jiao, Y. Qian, C. Y. Pan, L. Zheng, X. Cai, B. Liu, S. H. Yu and H. L. Jiang, *Angew. Chem., Int. Ed.*, 2020, **59**, 2705–2709.

35 Y. Zhou, R. Abazari, J. Chen, M. Tahir, A. Kumar, R. R. Ikreedeegh, E. Rani, H. Singh and A. M. Kirillov, *Coord. Chem. Rev.*, 2022, **451**, 214264.

36 X. Liu, M. Zhuo, W. Zhang, M. Gao, X.-H. Liu, B. Sun and J. Wu, *Ultrason. Sonochem.*, 2020, **67**, 105179.

37 X.-H. Liu, W.-L. Hu, W.-J. Jiang, Y.-W. Yang, S. Niu, B. Sun, J. Wu and J.-S. Hu, *ACS Appl. Mater. Interfaces*, 2017, **9**, 28473–28477.

38 R. Díaz, M. G. Orcajo, J. A. Botas, G. Calleja and J. Palma, *Mater. Lett.*, 2012, **68**, 126–128.

39 Y. Yang and D. S. Sholl, *J. Mater. Chem. A*, 2022, **10**, 4242–4253.

40 K. Ren, X.-F. Guo, Y.-J. Tang, B.-H. Huang and H. Wang, *Analyst*, 2020, **145**, 7349–7356.

41 B. An, Z. Li, Y. Song, J. Zhang, L. Zeng, C. Wang and W. Lin, *Nat. Catal.*, 2019, **2**, 709–717.

42 B. Li, Z. Ju, M. Zhou, K. Su and D. Yuan, *Angew. Chem., Int. Ed.*, 2019, **58**, 7687–7691.

43 R. Chen, L. Cheng, J. Liu, Y. Wang, W. Ge, C. Xiao, H. Jiang, Y. Li and C. Li, *Small*, 2022, **18**, 2200720.

44 Y. Zhang, Q. Zhou, Z. F. Qiu, X. Y. Zhang, J. Q. Chen, Y. Zhao, F. Gong and W. Y. Sun, *Adv. Funct. Mater.*, 2022, **32**, 2203677.

45 M. Wen, N. Sun, L. Jiao, S. Q. Zang and H. L. Jiang, *Angew. Chem., Int. Ed.*, 2024, **63**, e202318338.

46 L. Jiao, J. Zhu, Y. Zhang, W. Yang, S. Zhou, A. Li, C. Xie, X. Zheng, W. Zhou and S.-H. Yu, *J. Am. Chem. Soc.*, 2021, **143**, 19417–19424.

47 Z. Jin, D. Jiao, Y. Dong, L. Liu, J. Fan, M. Gong, X. Ma, Y. Wang, W. Zhang and L. Zhang, *Angew. Chem., Int. Ed.*, 2024, **63**, e202318246.

48 Y. Zhang, L. Jiao, W. Yang, C. Xie and H. L. Jiang, *Angew. Chem., Int. Ed.*, 2021, **60**, 7607–7611.

49 L. L. Zhuo, P. Chen, K. Zheng, X. W. Zhang, J. X. Wu, D. Y. Lin, S. Y. Liu, Z. S. Wang, J. Y. Liu and D. D. Zhou, *Angew. Chem., Int. Ed.*, 2022, **61**, e202204967.

50 R. Iqbal, M. B. Akbar, A. Ahmad, A. Hussain, N. Altaf, S. Ibraheem, G. Yasin, M. A. Khan, M. Tabish and A. Kumar, *Adv. Mater. Interfaces*, 2022, **9**, 2101505.

51 Z. H. Zhu, Z. L. Liang, Z. H. Jiao, X. L. Jiang, Y. Xie, H. Xu and B. Zhao, *Angew. Chem., Int. Ed.*, 2022, **61**, e202214243.

52 P. Lamagni, M. Miola, J. Catalano, M. S. Hvid, M. A. H. Mamakhel, M. Christensen, M. R. Madsen, H. S. Jeppesen, X. M. Hu and K. Daasbjerg, *Adv. Funct. Mater.*, 2020, **30**, 1910408.

53 Q. Mo, S. Li, C. Chen, H. Song, Q. Gao and L. Zhang, *ACS Sustainable Chem. Eng.*, 2024, **12**, 6093–6101.

54 T. Zhang, X. Han, H. Liu, M. Biset-Peiró, J. Li, X. Zhang, P. Tang, B. Yang, L. Zheng and J. R. Morante, *Adv. Funct. Mater.*, 2022, **32**, 2111446.

55 Y. Zhang, Y.-Y. Xing, C. Wang, R. Pang, W.-W. Ren, S. Wang, Z.-M. Li, L. Yang, W.-C. Tong and Q.-Y. Wang, *ACS Appl. Mater. Interfaces*, 2022, **14**, 23909–23915.

56 T. Zhao, H. Wu, X. Wen, J. Zhang, H. Tang, Y. Deng, S. Liao and X. Tian, *Coord. Chem. Rev.*, 2022, **468**, 214642.

57 X. Wang, Z. Chen, X. Zhao, T. Yao, W. Chen, R. You, C. Zhao, G. Wu, J. Wang and W. Huang, *Angew. Chem., Int. Ed.*, 2018, **57**, 1944–1948.

58 Y. Zhang, Q. Zhou, Z. F. Qiu, X. Y. Zhang, J. Q. Chen, Y. Zhao, F. Gong and W. Y. Sun, *Adv. Funct. Mater.*, 2022, **32**, 2203677.

59 J. Li, G. Chen, Y. Zhu, Z. Liang, A. Pei, C.-L. Wu, H. Wang, H. R. Lee, K. Liu and S. Chu, *Nat. Catal.*, 2018, **1**, 592–600.

60 C. Genovese, M. E. Schuster, E. K. Gibson, D. Gianolio, V. Posligua, R. Grau-Crespo, G. Cibin, P. P. Wells, D. Garai and V. Solokha, *Nat. Commun.*, 2018, **9**, 935.

61 A. R. Woldu, Z. Huang, P. Zhao, L. Hu and D. Astruc, *Coord. Chem. Rev.*, 2022, **454**, 214340.

62 J. Yu, J. Wang, Y. Ma, J. Zhou, Y. Wang, P. Lu, J. Yin, R. Ye, Z. Zhu and Z. Fan, *Adv. Funct. Mater.*, 2021, **31**, 2102151.

63 K. P. Kuhl, E. R. Cave, D. N. Abram and T. F. Jaramillo, *Energy Environ. Sci.*, 2012, **5**, 7050–7059.

64 R. K. Aparna, V. Surendran, D. Roy, B. Pathak, M. M. Shaijumon and S. Mandal, *ACS Appl. Energy Mater.*, 2023, **6**, 4072–4078.

65 Y. Wang, B. J. Park, V. K. Paidi, R. Huang, Y. Lee, K.-J. Noh, K.-S. Lee and J. W. Han, *ACS Energy Lett.*, 2022, **7**, 640–649.

66 X. Jiang, H. Li, J. Xiao, D. Gao, R. Si, F. Yang, Y. Li, G. Wang and X. Bao, *Nano Energy*, 2018, **52**, 345–350.

67 Z. Meng, J. Luo, W. Li and K. A. Mirica, *J. Am. Chem. Soc.*, 2020, **142**, 21656–21669.

68 H. Zhong, M. Ghorbani-Asl, K. H. Ly, J. Zhang, J. Ge, M. Wang, Z. Liao, D. Makarov, E. Zschech and E. Brunner, *Nat. Commun.*, 2020, **11**, 1409.

69 J. H. Cho, C. Lee, S. H. Hong, H. Y. Jang, S. Back, M. g. Seo, M. Lee, H. K. Min, Y. Choi and Y. J. Jang, *Adv. Mater.*, 2023, **35**, 2208224.

70 T. Wen, M. Liu, S. Chen, Q. Li, Y. Du, T. Zhou, C. Ritchie and J. Zhang, *Small*, 2020, **16**, 1907669.

71 S. Dou, J. Song, S. Xi, Y. Du, J. Wang, Z. F. Huang, Z. J. Xu and X. Wang, *Angew. Chem., Int. Ed.*, 2019, **58**, 4041–4045.

72 R. Shimoni, Z. Shi, S. Binyamin, Y. Yang, I. Liberman, R. Ifraemov, S. Mukhopadhyay, L. Zhang and I. Hod, *Angew. Chem., Int. Ed.*, 2022, **61**, e202206085.

73 Z. Zhang, J. Zhu, S. Chen, W. Sun and D. Wang, *Angew. Chem., Int. Ed.*, 2023, **62**, e202215136.

20602 | *J. Mater. Chem. A*, 2024, **12**, 20578–20605

This journal is © The Royal Society of Chemistry 2024

74 H. Li, X. Liu, S. Chen, D. Yang, Q. Zhang, L. Song, H. Xiao, Q. Zhang, L. Gu and X. Wang, *Adv. Energy Mater.*, 2019, **9**, 1900072.

75 F. Pan, H. Zhang, K. Liu, D. Cullen, K. More, M. Wang, Z. Feng, G. Wang, G. Wu and Y. Li, *ACS Catal.*, 2018, **8**, 3116–3122.

76 Z. Li, J. Jiang, X. Liu, Z. Zhu, J. Wang, Q. He, Q. Kong, X. Niu, J. S. Chen and J. Wang, *Small*, 2022, **18**, 2203495.

77 D.-H. Nam, O. Shekhah, G. Lee, A. Mallick, H. Jiang, F. Li, B. Chen, J. Wicks, M. Eddaoudi and E. H. Sargent, *J. Am. Chem. Soc.*, 2020, **142**, 21513–21521.

78 T. A. Al-Attas, N. N. Marei, X. Yong, N. G. Yasri, V. Thangadurai, G. Shimizu, S. Siahrostami and M. G. Kibria, *ACS Catal.*, 2021, **11**, 7350–7357.

79 X. Wang, Z. Chen, X. Zhao, T. Yao, W. Chen, R. You, C. Zhao, G. Wu, J. Wang and W. Huang, *Angew. Chem., Int. Ed.*, 2018, **130**, 1962–1966.

80 X. Yang, J. Cheng, H. Lv, X. Yang, L. Ding, Y. Xu, K. Zhang, W. Sun and J. Zhou, *Chem. Eng. J.*, 2022, **450**, 137950.

81 X. Zhang, Y. Zhang, Q. Li, X. Zhou, Q. Li, J. Yi, Y. Liu and J. Zhang, *J. Mater. Chem. A*, 2020, **8**, 9776–9787.

82 Y. Y. Liu, J. R. Huang, H. L. Zhu, P. Q. Liao and X. M. Chen, *Angew. Chem., Int. Ed.*, 2023, **62**, e202311265.

83 P. Song, B. Hu, D. Zhao, J. Fu, X. Su, W. Feng, K. Yu, S. Liu, J. Zhang and C. Chen, *ACS Nano*, 2023, **17**, 4619–4628.

84 Z. Xin, Y.-R. Wang, Y. Chen, W.-L. Li, L.-Z. Dong and Y.-Q. Lan, *Nano Energy*, 2020, **67**, 104233.

85 R. Yun, R. Xu, C. Shi, B. Zhang, T. Li, L. He, T. Sheng and Z. Chen, *Nano Res.*, 2023, **16**, 1–7.

86 Y. Li, W. Shan, M. J. Zachman, M. Wang, S. Hwang, H. Tabassum, J. Yang, X. Yang, S. Karakalos and Z. Feng, *Angew. Chem., Int. Ed.*, 2022, **61**, e202205632.

87 R. Yun, F. Zhan, X. Wang, B. Zhang, T. Sheng, Z. Xin, J. Mao, S. Liu and B. Zheng, *Small*, 2021, **17**, 2006951.

88 Y. Yang, L. Chen, Z. Guo, S. Liu, P.-d. Wu, Z. Fang, K. Zhang and H. Li, *J. Mater. Chem. A*, 2024, **12**, 8991–9001.

89 J. W. Lim, D. H. Choo, J. H. Cho, J. Kim, W. S. Cho, O. F. N. Okello, K. Kim, S. Lee, J. Son and S.-Y. Choi, *J. Mater. Chem. A*, 2024, **12**, 11090–11100.

90 J. D. Yi, D. H. Si, R. Xie, Q. Yin, M. D. Zhang, Q. Wu, G. L. Chai, Y. B. Huang and R. Cao, *Angew. Chem., Int. Ed.*, 2021, **133**, 17108–17114.

91 L. L. Ling, L. Jiao, X. Liu, Y. Dong, W. Yang, H. Zhang, B. Ye, J. Chen and H. L. Jiang, *Adv. Mater.*, 2022, **34**, 2205933.

92 M. Feng, X. Wu, H. Cheng, Z. Fan, X. Li, F. Cui, S. Fan, Y. Dai, G. Lei and G. He, *J. Mater. Chem. A*, 2021, **9**, 23817–23827.

93 H. Cheng, X. Wu, M. Feng, X. Li, G. Lei, Z. Fan, D. Pan, F. Cui and G. He, *ACS Catal.*, 2021, **11**, 12673–12681.

94 F. Mao, Y.-H. Jin, P. F. Liu, P. Yang, L. Zhang, L. Chen, X.-M. Cao, J. Gu and H. G. Yang, *J. Mater. Chem. A*, 2019, **7**, 23055–23063.

95 C. Hu, W. Yao, X. Yang, K. Shen, L. Chen and Y. Li, *Adv. Sci.*, 2024, **11**, 2306095.

96 C. Hu, Y. Zhang, A. Hu, Y. Wang, X. Wei, K. Shen, L. Chen and Y. Li, *Adv. Mater.*, 2023, **35**, 2209298.

97 Y. Takaoka, J. T. Song, A. Takagaki, M. Watanabe and T. Ishihara, *Appl. Catal., B*, 2023, **326**, 122400.

98 S.-Z. Hou, X.-D. Zhang, W.-W. Yuan, Y.-X. Li and Z.-Y. Gu, *Inorg. Chem.*, 2020, **59**, 11298–11304.

99 Y. Zhou, S. Liu, Y. Gu, G.-H. Wen, J. Ma, J.-L. Zuo and M. Ding, *J. Am. Chem. Soc.*, 2021, **143**, 14071–14076.

100 Z.-H. Zhao, J.-R. Huang, D.-S. Huang, H.-L. Zhu, P.-Q. Liao and X.-M. Chen, *J. Am. Chem. Soc.*, 2024, **146**, 14349–14356.

101 Y. Yang, J. Huang, Y. Zou, Y. Li, T. Zhan, L. Huang, X. Ma, Z. Zhang and S. Xiang, *Appl. Surf. Sci.*, 2023, **618**, 156664.

102 Z. Jiang, M. Zhang, X. Chen, B. Wang, W. Fan, C. Yang, X. Yang, Z. Zhang, X. Yang and C. Li, *Angew. Chem., Int. Ed.*, 2023, **62**, e202311223.

103 R. Yang, Q. Huang, X. Sha, B. Gao and J. Peng, *Int. J. Mol. Sci.*, 2023, **24**, 13838.

104 D. Yao, C. Tang, A. Vasileff, X. Zhi, Y. Jiao and S. Z. Qiao, *Angew. Chem., Int. Ed.*, 2021, **60**, 18178–18184.

105 S. Ma, K. Wu, S. Fan, Y. Li, Q. Xie, J. Ma and L. Yang, *Sep. Purif. Technol.*, 2024, **339**, 126520.

106 Z. Gao, M. Hou, Y. Shi, L. Li, Q. Sun, S. Yang, Z. Jiang, W. Yang, Z. Zhang and W. Hu, *Chem. Sci.*, 2023, **14**, 6860–6866.

107 L. Mi, B. Chen, X. Xu, S. Cai, Y. He, Y. Wei, Y. Jiang, C. Zheng, S. Zhong and W. Hu, *J. Alloys Compd.*, 2024, **978**, 173516.

108 Q. Huang, X. Sha, R. Yang, H. Li and J. Peng, *ACS Appl. Mater. Interfaces*, 2024, **16**, 13882–13892.

109 Y. Zhang, S. Liu, N. Ji, L. Wei, Q. Liang, J. Li, Z. Tian, J. Su and Q. Chen, *J. Mater. Chem. A*, 2024, **12**, 7528–7535.

110 C. Qiu, K. Qian, J. Yu, M. Sun, S. Cao, J. Gao, R. Yu, L. Fang, Y. Yao and X. Lu, *Nano-Micro Lett.*, 2022, **14**, 167.

111 C. Cao, D. D. Ma, J. F. Gu, X. Xie, G. Zeng, X. Li, S. G. Han, Q. L. Zhu, X. T. Wu and Q. Xu, *Angew. Chem., Int. Ed.*, 2020, **59**, 15014–15020.

112 Y. Zhang, Q. Zhou, P. Wang, Y. Zhao, F. Gong and W. Y. Sun, *ChemSusChem*, 2022, **15**, e202102528.

113 G. Liu, Q. T. Trinh, H. Wang, S. Wu, J. M. Arce-Ramos, M. B. Sullivan, M. Kraft, J. W. Ager, J. Zhang and R. Xu, *Small*, 2023, 2301379.

114 Y.-Y. Liu, H.-L. Zhu, Z.-H. Zhao, N.-Y. Huang, P.-Q. Liao and X.-M. Chen, *ACS Catal.*, 2022, **12**, 2749–2755.

115 X. Tan, C. Yu, C. Zhao, H. Huang, X. Yao, X. Han, W. Guo, S. Cui, H. Huang and J. Qiu, *ACS Appl. Mater. Interfaces*, 2019, **11**, 9904–9910.

116 J. Lv, W. Li, J. Li, Z. Zhu, A. Dong, H. Lv, P. Li and B. Wang, *Angew. Chem., Int. Ed.*, 2023, **62**, e202217958.

117 Y. L. Yang, Y. R. Wang, L. Z. Dong, Q. Li, L. Zhang, J. Zhou, S. N. Sun, H. M. Ding, Y. Chen and S. L. Li, *Adv. Mater.*, 2022, **34**, 2206706.

118 Y. Liu, S. Li, L. Dai, J. Li, J. Lv, Z. Zhu, A. Yin, P. Li and B. Wang, *Angew. Chem., Int. Ed.*, 2021, **60**, 16409–16415.

119 Y. Zhang, X.-Y. Zhang and W.-Y. Sun, *ACS Catal.*, 2023, **13**, 1545–1553.

120 S. Chen, W. H. Li, W. Jiang, J. Yang, J. Zhu, L. Wang, H. Ou, Z. Zhuang, M. Chen and X. Sun, *Angew. Chem., Int. Ed.*, 2022, **61**, e202114450.

This journal is © The Royal Society of Chemistry 2024

J. Mater. Chem. A, 2024, **12**, 20578–20605 | **20603**

121 H.-L. Zhu, J.-R. Huang, X.-W. Zhang, C. Wang, N.-Y. Huang, P.-Q. Liao and X.-M. Chen, *ACS Catal.*, 2021, **11**, 11786–11792.

122 P. Shao, W. Zhou, Q. L. Hong, L. Yi, L. Zheng, W. Wang, H. X. Zhang, H. Zhang and J. Zhang, *Angew. Chem., Int. Ed.*, 2021, **60**, 16687–16692.

123 T. Yan, J.-H. Guo, Z.-Q. Liu and W.-Y. Sun, *ACS Appl. Mater. Interfaces*, 2021, **13**, 25937–25945.

124 X.-D. Zhang, J.-M. Huang, X. Zhu, C. Liu, Y. Yin, J.-Y. Huang, Y. Li and Z.-Y. Gu, *Chin. Chem. Lett.*, 2024, 109937.

125 T. Yan, P. Wang and W. Y. Sun, *Small*, 2023, **19**, 2206070.

126 D. H. Nam, O. Shekhah, A. Ozden, C. McCallum, F. Li, X. Wang, Y. Lum, T. Lee, J. Li and J. Wicks, *Adv. Mater.*, 2022, **34**, 2207088.

127 X.-F. Qiu, H.-L. Zhu, J.-R. Huang, P.-Q. Liao and X.-M. Chen, *J. Am. Chem. Soc.*, 2021, **143**, 7242–7246.

128 D.-S. Huang, H.-L. Zhu, Z.-H. Zhao, J.-R. Huang, P.-Q. Liao and X.-M. Chen, *ACS Catal.*, 2022, **12**, 8444–8450.

129 Z.-H. Zhao, H.-L. Zhu, J.-R. Huang, P.-Q. Liao and X.-M. Chen, *ACS Catal.*, 2022, **12**, 7986–7993.

130 J. Wang, J. Liu, Y. Song, S. Geng, Z. Peng, J. Yu, F. Liu, Y. Wang, S. Xi and Z. Zhang, *ACS Mater. Lett.*, 2023, **5**, 2121–2130.

131 J. Feng, W. Zhang, D. Shi, Y. Jia, Y. Tang, Y. Meng and Q. Gao, *Chem. Sci.*, 2024, **15**, 9173–9182.

132 C. F. Wen, M. Zhou, P. F. Liu, Y. Liu, X. Wu, F. Mao, S. Dai, B. Xu, X. L. Wang and Z. Jiang, *Angew. Chem., Int. Ed.*, 2022, **61**, e202111700.

133 H. Sun, L. Chen, L. Xiong, K. Feng, Y. Chen, X. Zhang, X. Yuan, B. Yang, Z. Deng and Y. Liu, *Nat. Commun.*, 2021, **12**, 6823.

134 C. Liu, X.-D. Zhang, J.-M. Huang, M.-X. Guan, M. Xu and Z.-Y. Gu, *ACS Catal.*, 2022, **12**, 15230–15240.

135 M. Kempasiddaiah, R. Samanta, S. Panigrahi, R. K. Trivedi, B. Chakraborty and S. Barman, *Nanoscale*, 2024, **16**, 10458–10473.

136 K. Zhao, Y. Liu, X. Quan, S. Chen and H. Yu, *ACS Appl. Mater. Interfaces*, 2017, **9**, 5302–5311.

137 X. Yang, J. Cheng, X. Yang, Y. Xu, W. Sun and J. Zhou, *Chem. Eng. J.*, 2022, **431**, 134171.

138 J. Liu, D. Yang, Y. Zhou, G. Zhang, G. Xing, Y. Liu, Y. Ma, O. Terasaki, S. Yang and L. Chen, *Angew. Chem., Int. Ed.*, 2021, **60**, 14473–14479.

139 C. Hu, Z. Jiang, Q. Wu, S. Cao, Q. Li, C. Chen, L. Yuan, Y. Wang, W. Yang and J. Yang, *Nat. Commun.*, 2023, **14**, 4767.

140 P. Lu, J. Lv, Y. Chen, Y. Ma, Y. Wang, W. Lyu, J. Yu, J. Zhou, J. Yin and Y. Xiong, *Nano Lett.*, 2024, **24**, 1553–1562.

141 S. Li, J. Yu, S. Zhang, W. Qiu, X. Tang, Z. Lin, R. Cai, Y. Fang, S. Yang and X. Cai, *Adv. Funct. Mater.*, 2024, **34**, 2311989.

142 W. Su, W. Guo and Y. Fan, *Chem. Eng. J.*, 2023, **477**, 147204.

143 Z.-H. Zhao, J.-R. Huang, P.-Q. Liao and X.-M. Chen, *J. Am. Chem. Soc.*, 2023, **149**, 26783–26790.

144 J. Liu, Y. Wang, P. Mo, F. Yang, K. Jiang, Z. Cheng, Y. Liu, Z. Sun, Z. Liu and Y. Zhang, *Nano Res.*, 2024, **17**, 3888–3894.

145 Y. Zhang, K. Li, M. Chen, J. Wang, J. Liu and Y. Zhang, *ACS Appl. Nano Mater.*, 2019, **3**, 257–263.

146 K. Zhao, X. Nie, H. Wang, S. Chen, X. Quan, H. Yu, W. Choi, G. Zhang, B. Kim and J. G. Chen, *Nat. Commun.*, 2020, **11**, 2455.

147 S. Payra, S. Kanungo and S. Roy, *Nanoscale*, 2022, **14**, 13352–13361.

148 Z. Tang, W. He, Y. Wang, Y. Wei, X. Yu, J. Xiong, X. Wang, X. Zhang, Z. Zhao and J. Liu, *Appl. Catal., B*, 2022, **311**, 121371.

149 W. Su, W. Guo and Y. Fan, *Chem. Eng. J.*, 2023, **147**, 147204.

150 Z.-H. Gao, K. Wei, T. Wu, J. Dong, D.-e. Jiang, S. Sun and L.-S. Wang, *J. Am. Chem. Soc.*, 2022, **144**, 5258–5262.

151 Y. Pan, R. Lin, Y. Chen, S. Liu, W. Zhu, X. Cao, W. Chen, K. Wu, W.-C. Cheong and Y. Wang, *J. Am. Chem. Soc.*, 2018, **140**, 4218–4221.

152 W. Xie, T. Yang, N. Tian, X.-H. Liu and J. Chen, *Energy Fuels*, 2022, **36**, 958–964.

153 H. Kim, D. Shin, W. Yang, D. H. Won, H.-S. Oh, M. W. Chung, D. Jeong, S. H. Kim, K. H. Chae and J. Y. Ryu, *J. Am. Chem. Soc.*, 2021, **143**, 925–933.

154 P. Wang, S. Meng, B. Zhang, M. He, P. Li, C. Yang, G. Li and Z. Li, *J. Am. Chem. Soc.*, 2023, **145**, 26133–26143.

155 R. Wang, J. Liu, L.-Z. Dong, J. Zhou, Q. Huang, Y.-R. Wang, J.-W. Shi and Y.-Q. Lan, *CCS Chem.*, 2023, **5**, 2237–2250.

156 Q. Lei, L. Huang, J. Yin, B. Davaasuren, Y. Yuan, X. Dong, Z.-P. Wu, X. Wang, K. X. Yao and X. Lu, *Nat. Commun.*, 2022, **13**, 4857.

157 Z. Jiang, T. Wang, J. Pei, H. Shang, D. Zhou, H. Li, J. Dong, Y. Wang, R. Cao and Z. Zhuang, *Energy Environ. Sci.*, 2020, **13**, 2856–2863.

158 Y. Zhao, L. Zheng, D. Jiang, W. Xia, X. Xu, Y. Yamauchi, J. Ge and J. Tang, *Small*, 2021, **17**, 2006590.

159 C. Cui, Q. Cao, H. Jing, Z. Zhao, D. Wang and Y. J. S. Li, *Surf. Interfaces*, 2024, **48**, 104353.

160 X. Peng, L. Zeng, D. Wang, Z. Liu, Y. Li, Z. Li, B. Yang, L. Lei, L. Dai and Y. Hou, *Chem. Soc. Rev.*, 2023, **52**, 2193–2237.

161 B. Zhang, Y. Jiang, M. Gao, T. Ma, W. Sun and H. Pan, *Nano Energy*, 2021, **80**, 105504.

162 K. A. Adegoke and N. W. Maxakato, *Coord. Chem. Rev.*, 2022, **457**, 214389.

163 H. Meng, Y. Han, C. Zhou, Q. Jiang, X. Shi, C. Zhan and R. Zhang, *Small Methods*, 2020, **4**, 2000396.

164 C. Li, L. Zhang, J. Chen, X. Li, J. Sun, J. Zhu, X. Wang and Y. Fu, *Nanoscale*, 2021, **13**, 485–509.

165 S. Mandal, S. Natarajan, P. Mani and A. Pankajakshan, *Adv. Funct. Mater.*, 2021, **31**, 2006291.

166 D.-W. Lim and H. Kitagawa, *Chem. Soc. Rev.*, 2021, **50**, 6349–6368.

167 J. Ye, J. Yan, Y. Peng, F. Li and J. Sun, *Catal. Today*, 2023, **410**, 68–84.

168 M. Tang, H. Shen and Q. Sun, *J. Phys. Chem. C*, 2019, **123**, 26460–26466.

169 Q. Cui, G. Qin, W. Wang, K. Geethalakshmi, A. Du and Q. Sun, *Appl. Surf. Sci.*, 2020, **500**, 143993.

170 Y. Tian, Y. Wang, L. Yan, J. Zhao and Z. Su, *Appl. Surf. Sci.*, 2019, **467**, 98–103.

20604 | *J. Mater. Chem. A*, 2024, **12**, 20578–20605

This journal is © The Royal Society of Chemistry 2024

171 G. Xing, L. Cheng, K. Li, Y. Gao, H. Tang, Y. Wang and Z. Wu, *New J. Chem.*, 2020, **44**, 12299–12306.

172 Y. Tian, C. Zhu, L. Yan, J. Zhao and Z. Su, *J. Mater. Chem. A*, 2019, **7**, 15341–15346.

173 H. Zhong, M. Wang, G. Chen, R. Dong and X. Feng, *ACS Nano*, 2022, **16**, 1759–1780.

174 L. Majidi, A. Ahmadiparidari, N. Shan, S. N. Misal, K. Kumar, Z. Huang, S. Rastegar, Z. Hemmat, X. Zou and P. Zapol, *Adv. Mater.*, 2021, **33**, 2004393.

175 J. Liu, D. Yang, Y. Zhou, G. Zhang, G. Xing, Y. Liu, Y. Ma, O. Terasaki, S. Yang and L. Chen, *Angew. Chem., Int. Ed.*, 2021, **60**, 14473–14479.

176 L. Huang, Z. Liu, G. Gao, C. Chen, Y. Xue, J. Zhao, Q. Lei, M. Jin, C. Zhu and Y. Han, *J. Am. Chem. Soc.*, 2023, **145**, 26444–26451.

177 M. G. Lee, S. Kandambeth, X.-Y. Li, O. Shekhah, A. Ozden, J. Wicks, P. Ou, S. Wang, R. Dorakhan and S. Park, *J. Am. Chem. Soc.*, 2024, **146**, 14267–14277.

178 Z.-Z. Wu, F.-Y. Gao and M.-R. Gao, *Energy Environ. Sci.*, 2021, **14**, 1121–1139.

179 Q. Fan, X. Zhang, X. Ge, L. Bai, D. He, Y. Qu, C. Kong, J. Bi, D. Ding and Y. Cao, *Adv. Energy Mater.*, 2021, **11**, 2101424.

180 S. Li, A. V. Nagarajan, Y. Li, D. R. Kauffman, G. Mpourmpakis and R. Jin, *Nanoscale*, 2021, **13**, 2333–2337.

181 X.-L. Lv, L. Feng, L.-H. Xie, T. He, W. Wu, K.-Y. Wang, G. Si, B. Wang, J.-R. Li and H.-C. Zhou, *J. Am. Chem. Soc.*, 2021, **143**, 2784–2791.

182 X. Cheng, J. Zhang, X. Tan, L. Zheng, D. Tan, L. Liu, G. Chen, Q. Wan, B. Zhang and F. Zhang, *Chem. Commun.*, 2020, **56**, 7637–7640.

183 X. Mao, W. Gong, Y. Fu, J. Li, X. Wang, A. P. O'Mullane, Y. Xiong and A. Du, *J. Am. Chem. Soc.*, 2023, **145**, 21442–21453.

184 A. K. Singh, L. Gu, A. Dutta Chowdhury and A. Indra, *Inorg. Chem.*, 2023, **62**, 8803–8811.

185 T. Al-Attas, S. K. Nabil, A. S. Zeraati, H. S. Shiran, T. Alkayyali, M. Zargartalebi, T. Tran, N. N. Marei, M. A. Al Bari and H. Lin, *ACS Energy Lett.*, 2022, **8**, 107–115.

186 A. Bencini and V. Lippolis, *Coord. Chem. Rev.*, 2010, **254**, 2096–2180.

187 J. Wang, X. Huang, S. Xi, H. Xu and X. Wang, *Angew. Chem., Int. Ed.*, 2020, **59**, 19162–19167.

188 X. Xie, X. Zhang, M. Xie, L. Xiong, H. Sun, Y. Lu, Q. Mu, M. H. Rummeli, J. Xu, S. Li, J. Zhong, Z. Deng, B. Ma, T. Cheng, W. A. Goddard and Y. Peng, *Nat. Commun.*, 2022, **13**, 63.

189 Z. Xin, J. Liu, X. Wang, K. Shen, Z. Yuan, Y. Chen and Y.-Q. Lan, *ACS Appl. Mater. Interfaces*, 2021, **13**, 54959–54966.

190 J. Deng, L. Qiu, M. Xin, W. He, W. Zhao, J. Dong and G. Xu, *Small*, 2024, 2311060.

191 C.-Y. Yuan, L. Feng, X.-T. Qin, J.-X. Liu, X. Li, X.-C. Sun, X.-X. Chang, B.-J. Xu, W.-X. Li and D. Ma, *Angew. Chem., Int. Ed.*, 2024, e202405255.

192 F. Chang, K. Zhu, C. Liu, J. Wei, S. Yang, Q. Zhang, L. Yang, X. Wang and Z. Bai, *Adv. Funct. Mater.*, 2024, 2400893.

193 C. Jia, Y. Zhao, S. Song, Q. Sun, Q. Meyer, S. Liu, Y. Shen and C. Zhao, *Adv. Energy Mater.*, 2023, **13**, 2302007.

194 P. Su, K. Iwase, S. Nakanishi, K. Hashimoto and K. Kamiya, *Small*, 2016, **12**, 6083–6089.

195 Z. Qi, Y. Zhou, R. Guan, Y. Fu and J. B. Baek, *Adv. Mater.*, 2023, **35**, 2210575.

196 B. Pan, X. Zhu, Y. Wu, T. Liu, X. Bi, K. Feng, N. Han, J. Zhong, J. Lu and Y. Li, *Adv. Sci.*, 2020, **7**, 2001002.

197 M. Qu, Z. Chen, Z. Sun, D. Zhou, W. Xu, H. Tang, H. Gu, T. Liang, P. Hu and G. J. N. R. Li, *Nano Res.*, 2023, **16**, 2170–2176.

198 S. Liu, L. Wang, H. Yang, S. Gao, Y. Liu, S. Zhang, Y. Chen, X. Liu and J. Luo, *Small*, 2022, **18**, 2104965.

199 X. Zhang, X. Sun, S.-X. Guo, A. M. Bond and J. Zhang, *Energy Environ. Sci.*, 2019, **12**, 1334–1340.

200 N. Han, Y. Wang, H. Yang, J. Deng, J. Wu, Y. Li and Y. Li, *Nat. Commun.*, 2018, **9**, 1320.

201 J. P. Jones, G. S. Prakash and G. A. Olah, *Isr. J. Chem.*, 2014, **54**, 1451–1466.

202 Q. Huang, X. Sha, R. Yang, H. Li and J. Peng, *ACS Appl. Mater. Interfaces*, 2024, **16**, 13882–13892.

203 W. He, I. Liberman, I. Rozenberg, R. Ifraemov and I. Hod, *Angew. Chem., Int. Ed.*, 2020, **59**, 8262–8269.

204 W. Zhang, C. Huang, J. Zhu, Q. Zhou, R. Yu, Y. Wang, P. An, J. Zhang, M. Qiu and L. Zhou, *Angew. Chem., Int. Ed.*, 2022, **61**, e202112116.

205 W. Zhang, Y. Yang, Y. Tang and Q. Gao, *J. Energy Chem.*, 2022, **70**, 414–436.

206 P. Liu, P. Jing, X. Xu, B. Liu and J. Zhang, *ACS Appl. Energy Mater.*, 2021, **4**, 12128–12136.

207 C. Bressler and M. Chergui, *Chem. Rev.*, 2004, **104**, 1781–1812.

208 K. Adarsh, N. Chandrasekaran and V. Chakrapani, *Front. Chem.*, 2020, **8**, 137.

209 S. Liu, L. Song, R. Liu, L. Li, D. Yang, S. Yuan and X. Dai, *Small*, 2023, **19**, 2304808.

210 C. Farber, J. Li, E. Hager, R. Chemelewski, J. Mullet, A. Y. Rogachev and D. Kurouski, *ACS Omega*, 2019, **4**, 3700–3707.

211 M. R. Smith, C. B. Martin, S. Arumuganainar, A. Gilman, B. E. Koel and M. L. Sarazen, *Angew. Chem., Int. Ed.*, 2023, **62**, e202218208.

212 G. Hai, X. Xue, S. Feng, Y. Ma and X. Huang, *ACS Catal.*, 2022, **12**, 15271–15281.

This journal is © The Royal Society of Chemistry 2024

J. Mater. Chem. A, 2024, **12**, 20578–20605 | **20605**